X-RAY FLUORESCENCE MEASUREMENTS OF MOLTEN ALUMINUM ELEMENTAL COMPOSITION

By: Leigh C. Duren

A Thesis Submitted to the Faculty of

WORCESTER POLYTECHNIC INSTITUTE

in partial fulfillment of the requirements for the

Degree of Master of Science

in

Materials Science and Engineering

December 2007

APPROVED BY:

Dr. Diran Apelian, Advisor

Dr. Daniel Backman, Co-Advisor

Dr. Richard D. Sisson, Jr., Director, Materials Science and Engineering

Abstract

The aluminum industry is in need of high-speed in-situ elemental identification technology for molten metals. wTe Corporation of Bedford, MA was granted funds to research this technology for aluminum through the Advanced Technology Program (ATP) of the National Institute of Standards and Technology (NIST). As a secondary metal scrap processor, wTe Corporation is interested in increasing the value of scrap and better identification technology is one way of doing this. With better identification technology, foundries and smelters will be more confident in the melt chemistry and more apt to use secondary aluminum which decreases the energy required for processing by approximately 85%. wTe Corporation is exploring two avenues for in-situ molten metal identification: Laser Induced Breakdown Spectroscopy (LIBS) and X-Ray Fluorescence (XRF). The objectives of this work were to contribute to developing XRF technology for in-situ identification of molten metal by establishing a method of data instrumentation and analysis for XRF to determine aluminum melt composition, investigate the major alloying elements in the Al380 alloy series and determine the relationship between intensity and concentration, and to determine the effect of temperature on XRF Spectra. The XRF instrumentation development and the technical challenges associated with high temperature measurements are presented. The relationship between intensity and concentration is presented for three alloys within the 380 alloy series, and lastly it is observed that there are significant differences between liquid and solid spectra and that a calibration curve for liquid data is necessary. Several hypotheses are given as to why this difference between liquid and solid state spectra may occur.

Acknowledgements

I would like to gratefully acknowledge Dr. David Spencer, the found of wTe Corporation, for providing the funding for this project as well as valuable technical advice. I would like to thank Professor Diran Apelian for providing me with the opportunity to work on this project and for his guidance throughout. Thank you to Professor Daniel Backman for guidance as well as time spent in the lab running trials. This project was part of a much larger project and I thoroughly enjoyed working with the team at wTe Corporation: Leigh Peritz, Aldo Reti, Charlie Faulstich, and Jeff Webster as well as those at Energy Research Corporation: Robert DeSaro and Joe Crapero. I would also like to acknowledge Dr. Jean-Louis Staudenmann from the National Institute of Standards and Technology (NIST) Advanced Technology Program (ATP) who was the technical advisor to the entire team. Finally, I would like to acknowledge Carol Garofoli, Todor Kiryazov, and Maureen Plunkett of the Metal Processing Institute for their support throughout the project.

Table of Contents

List of Figures

List of Tables

1. Introduction

This chapter introduces the National Institute of Standards and Technology (NIST) Advanced Technology Program (ATP) to which this thesis contributes. It gives the reader background on the motivation of the performing organization, wTe Corporation of Bedford, MA, and explains the contribution of each of the participating companies to the goals of the ATP project.

wTe Corporation (wTe) is a 25-year old value added recycling company in Bedford, MA with both a plastics and metals division which processes secondary scrap. wTe has been successful in the market because they are committed to developing new technologies serving the metals recycling market. Over the past ten years they have raised almost $10.0 million in federal funds to develop a family of technologies for high speed sorting of metals and *in situ* identification of molten metal.

Most recently, wTe applied for funding through the NIST ATP. The ATP was formed to bridge the gap between the lab and commercial markets, promoting prosperity through innovation focusing on the needs of industry and not those of the government. More information about ATP can be found on their website, www.atp.nist.gov. The specific ATP project title is Optoelectronic Sensing of Liquid Metal Composition and the stated mission of the program is to develop and show feasibility for an innovative sensor system that combines real time integrated X-Ray fluorescence (XRF) and laser induced breakdown spectroscopy (LIBS). The motivation for the project is that off-line analysis of molten metal leads to excessive melting times, product quality problems, wasted feedstock, dramatic increases in energy use, increased emissions, wasted product and, subsequently, excessive production of scrap. Today, there is no on-line alternative available for industry. As a secondary scrap producer, wTe is interested in increasing the value of secondary scrap and keeping the sorting and recycling in the US and curtailing the current trend of scrap processing in China. With in situ identification of composition, smelters would have more confidence in the composition of their melts and be less hesitant to use scrap. One can see how an on-line system would benefit both secondary scrap processors -such as wTe- by increasing the value of their product, and foundries by decreasing the time and therefore energy spent at keeping heats in the molten state.

With this ATP grant two technologies are being developed side by side, namely XRF and LIBS. LIBS is being developed by Energy Research Company (ERCo) of Staten Island, New York (www.er-co.com). And XRF technology is being developed by wTe (www.wte.com). At the finish the two technologies will be joined in order to exploit and merge the strong-points of each technologies into one technology that will provide high accuracy and precision. The fusion of the technologies will be performed by wTe, ERCo, and National Recovery Technologies (NRT) of Nashville, TN. The focus of this work is on developing XRF technology.

2. Objectives

This research seeks to contribute to developing combined XRF and LIBS technology for in situ compositional analysis of molten aluminum by focusing on XRF technology; specifically the research seeks to:

- Establish a method of instrumentation and data analysis for XRF to determine aluminum melt composition;
- Investigate alloys within the aluminum 380 series and determine the relationship between intensity and concentration for the major alloying elements: Si, Fe, Cu, and Zn;
- Understand how characteristic emission line intensities are converted to elemental concentration by use of background subtraction, least squares fitting, background correlation functions, separation of peak overlaps etc., in order to determine the most suitable calibration procedure;
- Determine the effect of temperature on XRF spectra.

3. Literature Review and Background

This chapter provides a comprehensive review of the technology currently being used to analyze aluminum and a description of the recycling industry of aluminum today. This literature review provides an argument that the aluminum industry has been in need of an on-line chemical analysis system based on references to current analytical methods and attempts at *in situ* analysis in the past. A basic introduction to XRF is given and the specific technical challenges associated with using XRF for molten aluminum analysis are discussed.

3.1. Current Analytical Methods for Compositional Analysis of Aluminum

Spark Optical Emission Spectroscopy (OES) is the industry standard for verifying melt chemistry; the industry standard is an off-line method. In order to perform spark OES, a small sample of the molten metal alloy is drawn off or ladled from the molten bath and poured into a cold steel mold made to the specifications of ASTM E716-94 Sampling Aluminum and Aluminum Alloys for Spectrochemical Analysis. The homogeneity of the melt is assumed to be representative of the overall volume of the melt in process. If the melt is not well mixed and homogenous, it is possible that this sample is not necessarily representative of the actual average chemistry of the melt. Next, the sample is allowed to solidify and is then transported to a machine shop where it is machined to the ASTM specified depth to find a surface that is representative of the melt and to produce a smooth surface necessary for subsequent analysis. This sampling and machining process must be conducted on every sample drawn from every melt furnace in the foundry any time an addition or change is made. The samples are then delivered to a chemical testing laboratory. In the laboratory, they are subjected to spark OES following ASTM E1251-04 Analysis of Aluminum and Aluminum Alloys by Atomic Emission Spectrometry. Alternatively, the solid sample at room temperature may be subjected to static X-Ray fluorescence analysis (XRF). If the sample does not fall within specified compositional tolerance levels, adjustments are made to the liquid melt and the process must necessarily be repeated until the final composition falls within the allowable compositional tolerance limits for the alloy being produced. Each time an addition is made, time must be allowed for convective mixing of the melt before another sample is drawn for analysis. Using secondary scrap as the initial charge can cause additional uncertainty in the composition and so, there is a reluctance to use the greatest amount of secondary scrap possible

Compositional adjustment is a very time consuming process that wastes considerable energy as it can take 45 minutes to 1-hour or more from the time an addition is made upon receipt of OES compositional results. The results are also subject to sampling error and macrosegregation. During sampling, the composition of a heat can change due to de-gassing, elemental fading (e.g. loss of strontium additions used for grain refining), and formation of intermetallic phases that form during melting. By the time the analysis is finalized the composition of the melt at the time of sampling may have changed. In today's industry where foundry profit margins are low and production quotas take priority, it is important to make melts as fast and as accurately as possible. Clearly, the current spark OES method creates significant potential for loss of product.

The current analytical methods for aluminum are off-line and require more time than is desirable causing excessive energy losses and higher cost.

3.2. The Aluminum Recycling Industry

Currently, much of the aluminum in the United States is hand sorted for recycling in China based on visual inspection as shown in Figure 1. Visual inspection allows for separation of aluminum from copper, or brass, or zinc, but separation between aluminum alloys themselves is not possible by visual inspection. The money and energy that is spent shipping these metals overseas for sortation is wasteful and there is a push from secondary scrap processors, such as wTe, to keep the sortation in the United States. In addition to the waste of shipping scrap overseas, Chinese workers are often paid unfairly at wages of 10 cents per day[1].

Figure 1: A Chinese metal sortation factory, the work of Adam Minter, an independent journalist and photographer based in Shanghai, China.[1]

Secondary aluminum produced from recycling products costs about 2.8kWh/kg of aluminum produced whereas primary aluminum processing requires about 45kWh/kg[2]. Secondary aluminum requires approximately 5% of the energy needed for primary processing, also emitting only 5% of CO_2 production as primary aluminum. In 2003 $1.72*10^{11}$ kWh were saved by using secondary scrap. Maximizing the amount of secondary scrap used in production will benefit scrap dealers by increasing demand and benefit foundries by decreasing processing costs.

wTe has committed to developing technologies that address both the sortation stage and melting stage of secondary aluminum production. With the development of these technologies many positive changes in the secondary aluminum market are expected. Spectrometry methods that can identify composition quickly in the solid and liquid state are needed.

3.3. An Introduction to X-Ray Fluorescence

X-Ray Fluorescent (XRF) compositional analysis has been a well established spectroscopic method since the late 1950s and many references and text books are available that describe the method. However, a brief synopsis is given below for the benefit of the reader who may be less familiar with XRF principles. The synopsis highlights only those particular elements of XRF spectroscopy that are important to this work and references one particular text book: Quantitative X-ray Spectrometry[3].

There are three fundamental ways that X-rays may interact with matter: they may be coherently scattered, incoherently scattered, or they may trigger the photoelectric effect; this latter effect serves as the basis for XRF. When an incident x-ray photon of sufficient energy interacts with an atom, its energy can be absorbed through the ejection of an inner shell electron. This reaction, termed the photoelectric effect, creates an electron vacancy and an ejected photoelectron but also destabilizes the atom. In reaction, a more loosely bound electron will fill the electron vacancy with the simultaneous emission of an x-ray photon or Auger electron from an outer electron shell. The emitted fluorescent x-ray photon (the more probable emission for elements of high atomic number) will have a characteristic energy equal to the difference in binding energies between the shell of the transitioning electron and the shell of the vacancy. These characteristic x-rays serve as the "fingerprint" for XRF analysis given that each element has a unique spectrum of electron energy levels and hence fluorescent x-ray photon energies. The fluorescence yield ω (a number between 0 and 1) describes the probability that a characteristic fluorescent x-ray will be emitted once a vacancy has been created as opposed to the emission of an Auger electron.

The interactions of x-rays with matter are described by the mass attenuation coefficient which is characteristic of the elements in the material. The mass attenuation coefficient μ(E) has units of (cm^2/g) where density ρ is given as (g/cm^3) and thickness is given in (cm). The mass attenuation coefficient is a lumped parameter that accounts for the photoelectric mass absorption coefficient, the total coherent mass scattering coefficient, and the total incoherent mass scattering coefficient and is a function of energy.

In XRF spectrometry, fluorescent characteristic energy is used for quantitative analysis. The conversion of the intensity of characteristic x-rays to elemental composition is both an art and a science that has employed strategies, approximations, and methods that have evolved over the past five decades. However, each serious analysis method has attempted to build upon the foundation provided by fundamental XRF principles as described by the equations below. The equations below are from Reference 3 and use fundamental parameters to describe the intensity of element i:

$$I_i(E_i)d\Omega_1 d\Omega_2 = d\Omega_1\left(\frac{d\Omega_2}{4\pi}\right)\frac{\eta(E_i)}{sin\varphi_1}\int_{E_{min}}^{E_{max}} Q_{if}(E_0)\times\left(\frac{1-\exp\{-\rho T[\mu(E_0)\csc\varphi_1+\mu(E_i)\csc\varphi_2]\}}{\mu(E_0)\csc\varphi_1+\mu(E_i)\csc\varphi_2}\right) \times I_0(E_0)dE_0$$

where:

$$Q_{if}(E_0) = W_i \tau_{Ki}(E_0) \omega_{Ki} f$$

The fundamental parameters used are described in Table 1.

Table 1: Fundamental parameters for converting line intensity to concentration

Symbols Used in the Fundamental Equation of XRF	
E_0	Primary radiation energy from the excitation source
E_i	Fluoresced radiation energy measured for the ith element
$I_0(E_0)dE_0$	Number of incident photons per second per steradian in energy interval E_0 to E_0+dE_0
$\mu(E_0)$	Total specimen mass attenuation coefficient for the energy E_0
$\mu(E_i)$	Total specimen mass attenuation coefficient for the fluoresced energy E_i
$\tau_{Ki}(E_0)$	Photoelectric mass absorption coefficient for the K shell of element i at the energy E_0
$Q_{if}(E_0)$	Fluorescence probability for measured line from element i
E_{max}	The maximum energy in the excitation spectrum
$\eta(E_i)$	The detection efficiency of the x-ray spectrometer for the fluoresced photons at energy E_i
$I_i(E_i)$	Number of detected fluoresced photons per second per steradian per steradian for the ith element at energy E_i
W_i	Weight fraction of element i
$d\Omega_1 d\Omega_2$	Solid angles in detector geometry
φ_1, φ_2	Effective incidence and takeoff angles, respectively
T	Specimen thickness
ω_{Ki}	Fluorescent yield for the K shell of element i at the energy E_0

This equation is very important to XRF spectroscopy; in order to perform quantitative analysis the integral over the entire primary excitation energy from the tube must be known. The equation shows that the fluorescence intensity of element i, $I_i(E_i)$, is proportional to:

- the weight fraction of element i in the specimen;
- the photoelectric mass absorption coefficient for element i;
- the fluorescence yield for element i;
- the detection efficiency for the fluoresced line energy.

The equation also reveals that the intensity is a function of the primary absorption $\mu(E_0)\csc\varphi_1$ and secondary absorption $\mu(E_0)\csc\varphi_2$ which are the major components of what are called matrix effects. Primary absorption reduces the effectiveness of x-rays from the primary source and secondary absorption reduces the intensity of the characteristic x-rays as the leave the specimen; secondary absorption is a function of all the other elements in the specimen. Enhancement is a third matrix effect caused by elements in the matrix whose characteristic energies lie to the high energy side of the absorption edges (energy necessary for ejecting an electron) of other elements within the matrix.

In summary, many parameters beyond the sample itself determine the measured intensity of a given element. In order to make the most accurate assessment of intensity, these parameters must be known and can be difficult to measure, or measure accurately. The reader who is interested in learning more about quantitative XRF should refer to Reference 3.

3.4.Technical Challenges Associated with XRF Analysis of Molten Aluminum

XRF has the potential to provide accurate and precise quantitative data for the chemical composition of molten aluminum. Liquids are actually the ideal specimen for analysis by XRF[4]. Liquids are homogeneous, particle effects are eliminated, and the obtained analytical results are representative of the whole sample. Even at room temperature, XRF can be a technically challenging and safety precautions must always be taken. Many of the technical challenges associated with XRF are amplified for high temperature measurements and some new technical challenges are introduced. These specific challenges are discussed below.

3.4.1. High Temperatures

The components of an XRF system are extremely sensitive to heat effects. Considering that Al melts at approximately 660^{o}C, XRF spectrometer components must be sufficiently isolated from the hot zone of the furnace and hot surface of the melt. In the harsh environment where the technology will be implemented there will also be significant amounts of radiative, convective, and conductive heating.

3.4.2. Harsh Environment

The environment in smelting and casting operations is extremely harsh. The presence of reducing and oxidizing atmospheres, dust and dirt, vibration, noise (both sound and electronic) can all have an adverse affect on the accuracy, maintenance and durability of an XRF system. Hardening an XRF system to operate in this type of environment will be a major challenge since the components in most XRF Spectrometers are fragile.

3.4.3. Varying Atmosphere

Since XRF energy is absorbed by the medium through which it travels by reduction of intensity through attenuation (particularly of low z elements), any differences in the composition and concentration of gases present in the space immediately above the molten metal will have an effect on the measurement. If this atmosphere is not made constant, it will be nearly impossible to generate analytical results on a consistent basis. Consideration must be taken on how to provide a constant atmosphere that will not attenuate the XRF signal.

3.4.4. Slag, Oxides, Dross and Surface Contamination

Surface contamination in molten metal is common. Some metals such as aluminum form an oxide layer almost immediately when in contact with air. Although an XRF system can penetrate through a thin layer of contaminants, the XRF from the contaminants themselves, especially in thicker layers, may bias the spectrum. Therefore, the accurate analysis of the elemental makeup of the molten metal may be problematic since the surface contaminant will be fluoresced in lieu of, or in addition to, the bulk metal being analyzed.

3.4.5. Geometry

For an accurate elemental analysis, particularly for elements of low concentration, the geometry of the components of an X-Ray system (detector and source) must be very well defined relative to the sample being analyzed. Accordingly, the elevation of the surface of the molten metal must be very accurately known and maintained during the analysis procedure. This will require a precise installation and a rigid structure to maintain that installation. This has the potential be difficult in the harsh environment of a metals melting operation.

3.4.6. Safety and Shielding

All equipment must be heavily shielded with X-Ray attenuating materials and safety interlocks must be built in to any radiative technology. Safety is critical as even short exposures to high energy X-Rays can be harmful or even fatal.

3.5.XRF Data for Liquid Metals

X-Ray and XRF data is essentially non-existent for liquid metals. We have found no data in the literature and there is no laboratory or commercial infrastructure. Based on theory, it is expected the XRF energy peaks to be the same for liquids and solids. However, with no liquid data available there is a need to develop this fundamental data.

3.6.Previous Works for In-Situ Molten Metal Analysis

There are few works sited for in-situ analysis of molten metal. Sited works include both XRF and LIBS work.

One such work was done by L. Creasy[5] at Axel Johnson Metals (now TIMET) in 1994. The work used the X-Rays created in an electron beam furnace and a wavelength dispersive X-Ray spectrometer designed to fit the furnace. The introduction to the article talks of the same motivation behind this project, namely the need for real-time analysis of molten metal to provide a more rapid chemistry acquisition. Additional information about the success and specifics of the system has not been published. Correspondence with the author by wTe indicated that this system was not for all elements in the melt, but only for specific alloying elements.

Beginning in 1995 there is mention of LIBS for analysis of molten metal, the motivation being savings in time, energy, and materials[6]. Paksy et. al[6] investigated methods for *in situ* analysis. In 2000, liquid steel analysis was performed by Gruber et. al[7] and Cr, Cu, Mn, and Ni were monitored within specified ranges. Additionally, in 2003 liquid aluminum measurements were taken and measurements were obtained for minor alloying elements using the ratio method to a major alloying element[8]. Also, significant research is being carried out currently at Energy Research Company (ERCo).

Although the idea for *in situ* analysis of molten metals is not a new one, none such analysis has been robust enough for commercialization and no attempt has been made at the fusion of two technologies in order to exploit the benefits of both. In-situ technology is needed to increase the value of secondary scrap and decrease the cost of processing for foundries. Both XRF and LIBS have the potential to provide precise and accurate data for all alloying elements in molten aluminum analysis and XRF is the focus of this work.

4. Methodology

To accomplish the stated objectives of this work and of the larger ATP program, specific protocol was taken to develop XRF testing equipment, design the experiments, and establish XRF procedures to be followed for every experiment.

4.1.Test Equipment Development

Because no readily available test equipment exists for the liquid measurement of XRF data, a melting furnace and XRF system was developed by the team under the ATP program. The system included a vacuum melting system capable of also operating under an inert helium environment and interfaces for the XRF components. It was imperative that the system be able to deliver an oxygen free environment so that the lab tests could be performed free of oxides and pristine data could be obtained. Development included selection of X-Ray source, X-Ray detector, and furnace design. The thermal management of the system was very important as well as the XRF components need to be shielded from excessive thermal and electromagnetic exposure.

4.2.Design of Experiments

An experimental plan that would results in completion of the objectives was designed using a 2-4 Half Fraction factorial with two additional added trials. The purpose of a factorial design is to study all possible combinations of two of more factors (in this case elements) at two levels (composition) to determine the effect that each factor has on the response variable (XRF intensity) as well as the interactions between factors. However, often factorial experiments require more trials than is feasible and so a fractional factorial design was selected. A fractional factorial design consists of a subset of the full factorial design. The factors are the weight percent of Si, Fe, Cu and Zn. The other elements in the matrix (Mn, Mg, Ni, and Sn) were kept constant. The two levels of the elements of interest are presented in Table 2.

Table 2: Levels used in half fraction factorial design

Element	Level 0 (wt%)	Level 1 (wt%)
Si	7.5	13.0
Fe	0.4	2.0
Cu	2.0	4.5
Zn	0.05	3.0

The fractional factorial design is presented in Table 3. One should notice that there are two levels of Zn, 3.00wt% and 0.3wt%. Initially, when the LLL, MMM, and HHH alloys were made the Zn Level 1 was selected as 0.30wt%. However, after the procurement of these alloys the level was changed to 3.0wt%. The experiments in this work were performed on the LLL, MMM, and HHH alloys which contain only 0.30wt% Zn.

Table 3: Fraction Factorial with Added Trails for X38X.X

Fraction Factorial with Added Trials					
	Element				
Melt	**Si**	**Fe**	**Cu**	**Zn**	**Mg**
LLL	7.50	0.40	2.00	0.05	0.15
2	13.00	0.40	2.00	3.00	0.15
3	7.50	2.00	2.00	3.00	0.15
4	13.00	2.00	2.00	0.05	0.15
5	7.50	0.40	4.50	3.00	0.15
6	13.00	0.40	4.50	0.05	0.15
7	7.50	2.00	4.50	0.05	0.15
8	13.00	2.00	4.50	3.00	0.15
9	7.50	2.00	2.00	0.05	5.50
10	13.00	0.40	4.50	3.00	5.50
MMM	10.00	1.00	3.25	0.15	0.15
HHH	13.00	2.00	4.50	0.30	0.15

The same melting practice (presented in detail in the next section) was used for all alloys and the target chemistry for the other alloying elements was Mn=0.25wt%, Ni=0.25wt%, and Sn=0.20wt% with the remaining balance all Al. The production order of each melt was randomized.

4.3.Melting Procedure for Preparation of Experimental Alloys

A 99.5% aluminum master alloy was used as it contained suitably low Fe for the proposed X38X.X matrix. It was judged that it would not be a problem if the limits of minor/trace alloying elements were below the listed composition of the LLL melt as long as they could be accurately measured with spark OES. For each melt, 80lbs were made in two separate 40lb heats. 50lbs of the 80lbs was sent to ERCo for analysis by LIBS. The team specified that the melts did not need to be degassed. To verify melt chemistry, samples were poured and analyzed according to ASTM E716 and E1251. When the melt chemistry was suitably close to the aim chemistry, each heat was poured as follows:

- one spark OES sample,
- a 2.5 cylindrical sample to be used for XRF,
- 20lbs of ingots were poured,
- a second spark OES sample,
- a 2.5lb cylindrical sample for XRF, a second 20lbs of ingots, and
- a final spark OES sample.

Spark OES samples were poured at the beginning, middle, and end of the heat so that the homogeneity of the melt could be verified.

The 2.5lb cylindrical samples provided two samples each after they were machined to fit in the crucibles used for XRF testing. The cylindrical samples were machined using a HAAS 3 axis CNC milling machine. The top of the sample was first milled into a smooth circle which was held by machined aluminum vice jaws. After this, the bottom of the casting was faced, machined into the correct sample size and engraved with a sample number indicating composition. The sample was then taken to a lathe, where the first sample was parted using a thin cutoff tool. The second sample was taken from the same casting using the same method. These were both placed back into the aluminum soft jaw vice, and faced to the same surface as the top bottom of each sample. The castings were then cleaned thoroughly, and inspected for proper size.

4.4.XRF Protocol

A protocol for melting and data acquisition was developed. This protocol was developed to ensure consistency between data acquisition, and to ensure that all data was taken in the liquid state. The melting schedule is shown in Table 4.

Table 4: Melt schedule for acquiring liquid XRF data

Step	Start Temperature (^{o}F)	Stop Temperature (^{o}F)	Duration (min)
1	70	300	10
2	300	300	15
Purge with Helium			
3	300	1300	30
4	1300	1300	5
5	1300	1300	60

Temperature measurements of the melt were made using Omega Type K thermocouples. XRF acquisition began at Step 5 directly after the temperature of the melt was recorded. Three 30 second liquid measurements were taken; one was taken during each of three successive 45 second intervals. A final temperature reading was taken directly after the last XRF spectrum was taken.

4.5. XRF Data Analysis

The data analysis for this ATP program is a two step process; the first step is to analyze data from a completely driven perspective and the second is to use commercial software which will require knowledge of first principles presented in the introduction about XRF. At this point, the ATP program is still in the first step and so a MatLab routine was developed to analyze the data. The MatLab routine fits normal distributions and subtracts backgrounds for the peaks of interest.

5. Results and Discussion

The results of this work are presented in this section. The results will contribute to the overall development of a potential commercial immersion XRF probe. Equipment development is a very important result and the developments of the equipment are presented below. The matrix effects of the LLL, MMM, and HHH alloy are investigated to be used in future work when fundamental parameters are used to convert intensity to elemental concentration. The results of the thermal profile of the melted sample are presented. The repeatability and normality of the spectra, the effect of data

acquisition time, and sample height were examined. Finally, an analysis of the liquid spectra is presented and a qualitative comparison is made for the differences observed between the solid and liquid spectra of samples. Hypotheses are presented for the possible causes of difference between liquid and solid spectra.

5.1. Equipment Development

Equipment development was a very important outcome of this work as no system for such work is currently available. High temperature required for melting aluminum alloys can only be controlled through integrated design of the furnace and XRF installation and consideration of material selection, heat shielding and cooling. The design placed the detector at a distance from the metal surface such that the thermal load was reduced while still providing an adequate X-Ray flux to the target and detector. The materials for the detector were investigated to ensure that the beryllium window and its adhesive could withstand the temperature. Heat shielding was integrated into the system to protect the XRF components during heat up. A closed loop water cooling system was integrated to provide cooling, and careful measures were taken to make sure that the cooling water and liquid sample could not mix and create an explosion.

The solution to the hostile operational environmental conditions involved isolating the equipment from conditions that may be present in an industrial setting such as excess vibration. For example, the water pump for the cooling system was placed outside the unit, which was later shown to increase the resolution of the XRF system.

One alternative to the varying condition of the atmosphere around the sensor was to control that atmosphere. This was done by modifying a vacuum induction furnace so that it could be purged with an inert gas, helium, after an initial vacuum cycle to remove most of the oxygen. Earlier XRF experiments with helium were successful because it is a light element that does not significantly attenuate XRF.

Slag, oxides and other surface contamination in molten metals have been and will continue to pose difficult problems. To minimize their occurrence, samples were CNC machined from a clean cylindrical casting to remove surface contamination. To minimize oxidation during melting the samples were always melted in a He atmosphere with 1ppmO_2 or less. Oxidation was minimized by first heating the sample to 300^{o}F in a vacuum to outgas the crucible, chamber, and sample surface and then the chamber cycled through a purge and vacuum cycle three times using laboratory grade helium.

To achieve consistent and optimal XRF geometry for varying samples, the detector and tube were placed in fixed positions and the sample was placed on a pedestal with 1” of travel distance accurate to a thousandth of an inch. With this configuration, the level of the molten metal could be precisely controlled.

Safety and shielding were ensured through both the wall thickness of the furnace chamber, which was sufficient to attenuate the X-Rays to very low levels and redundant electrical interlocks were designed into the system to prevent X-Ray tube operation when the chamber was open. In addition, to prevent any unauthorized use, the controller to activate X-Rays was removable and stored in a separate location from the X-Ray apparatus.

Operations, maintenance and calibration apply mainly to the final commercialization of the product, and this work will provide some of the necessary information for calibration. The hypothesis is that the equipment will require calibration and diagnosis from a remote, central location via the internet or dedicated network when it is installed in a commercial foundry.

After considering the following solutions presented above, the ATP program team concluded that a furnace capable of handling a range of metals including aluminum, copper, and ferrous alloys, compatible with XRF instruments, and capable of providing good atmosphere control was needed. The team contracted with Induction Atmospheres (IA) of Rochester, NY to build this furnace.

The equipment was fabricated by IA as an adaptation of their stock model vacuum induction furnace which consists of a bottom-loaded vacuum chamber, mechanical roughing and diffusion pumps, 8KW solid state induction power supply, vacuum gages, and controls, all contained within a 4 ft wide, by 3 ft deep by 6 ft high console. The custom unit is shown in Figure 2. The chamber is approximately 13 inches in diameter by 12 inches high and capable of hot zone operation at temperatures up to 2800°F.

Figure 2: Experimental XRF Unit

A schematic of the chamber and hot zone is shown in Figure 3. The hot zone lid pivots to cover the melt during heat up and expose the melt during XRF acquisition. The height of the crucible can be adjusted to the optimal height from a dial connected to the crucible pedestal which is sensitive to one-thousandth of an inch. Graphite crucibles were used in the experiments as they are less susceptible to cracking than aluminum-oxide crucibles. The thermocouples provide the user with the temperature directly outside of the melt, as well as providing the programmable logic controller with feedback on chamber temperature.

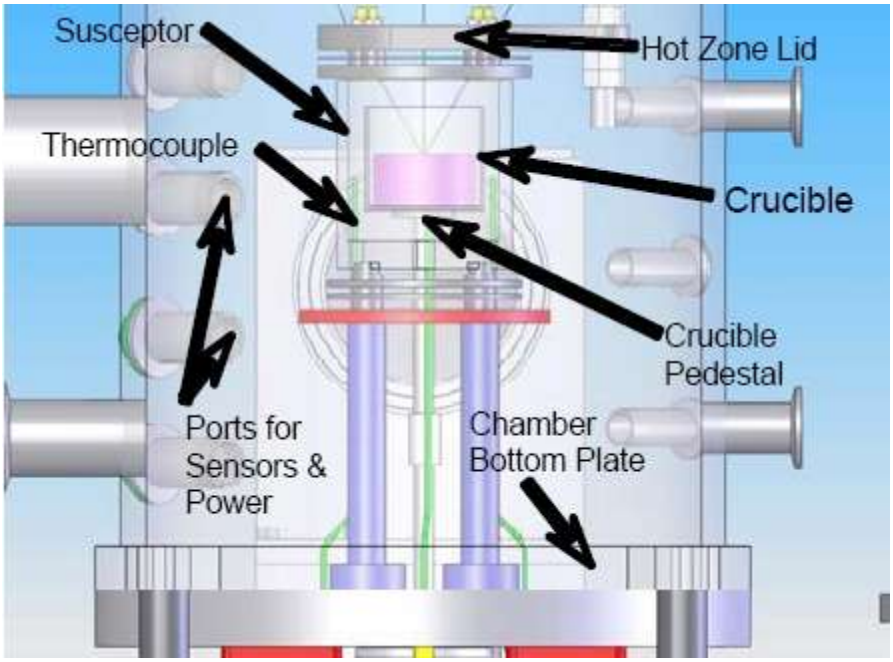

Figure 3: XRF Furnace Chamber Hot Zone

5.2. X-Ray Fluorescence Spectrometer

The X-Ray tube selected was a 75W (50kV x 1.5mA) X-Ray tube from Oxford. It has a side mounted beryllium window and a Rhodium target. The X-Ray detector used was the XR-100CR Si-PIN Photodiode detector from Amptek. This is a solid state detector and pre-amplifier which is cooled thermoelectrically. Thermoelectrically cooled detectors are relatively new and keep the components at approximately -55^{o}C providing performance that was previously only available from cryogenically cooled detectors. The detector has a Be window and 149eV resolution. The reader who wishes to learn more about the specifications of the XR-100CR should consult the specification sheet located in Appendix B: Specification Sheets for Experimental XRF Spectrometer. The multi-channel analyzer used was the PX-4 Digital Pulse Processor, also from Amptek. The PX-4 incorporates a digital pulse shaping amplifier, integrated multichannel analyzer, and power supplies. The reader who wishes to learn more about the PX-4 should again consult Appendix B: Specification Sheets for Experimental XRF Spectrometer.

5.3. X-Ray Tube Safety Assessment

X-Ray tubes and X-Ray detectors are not meant to operate at high temperatures and their functionality is dependent on operation within a narrow temperature window. Therefore, it was very important to ensure that the tube would remain protected and operate safely under the vacuum cycle and that the detector would remain at working temperature.

The Oxford X-Ray tube was identified as being a potential risk if leakage from the oil filled tube could rupture the beryllium window, drip into the hot chamber of the bench-top unit and create a dangerous over-pressure condition. While this risk was assessed to be unlikely, it was examined in greater detail since chamber over-pressurization could have a significant safety impact.

It was concluded that the risk is very remote, nonetheless the temperature of the X-Ray tube cooling oil was monitored. Temperature monitoring was concluded to be sufficient after examination of the X-Ray tube design, Figure 4, which shows that the oil chamber is structurally robust and isolated from the X-Ray generator (area containing the target, filament, Be window etc.). Also, during operation of the bench-top unit, the chamber contains either a vacuum or helium atmosphere such that if oil were to leak onto a hot surface within the chamber, it might vaporize but would not combust. IA also indicated that the major o-rings used to seal the chamber were designed for vacuum operation and would fail if the chamber were pressurized much above atmospheric pressure. Additionally, the bottom cover of the chamber is not bolted to the lower chamber flange but rather is held in a closed position using a pneumatic cylinder. Seal leakage or opening of the bottom seal would preclude the chamber from reaching explosive over-pressurization. In conclusion, the X-Ray tube condition is best gauged by closely monitoring oil temperature using the thermocouple provided as part of the tube assembly. It was judged that high oil temperature or abrupt oil temperature change would signal potential tube problems including internal or external oil leakage.

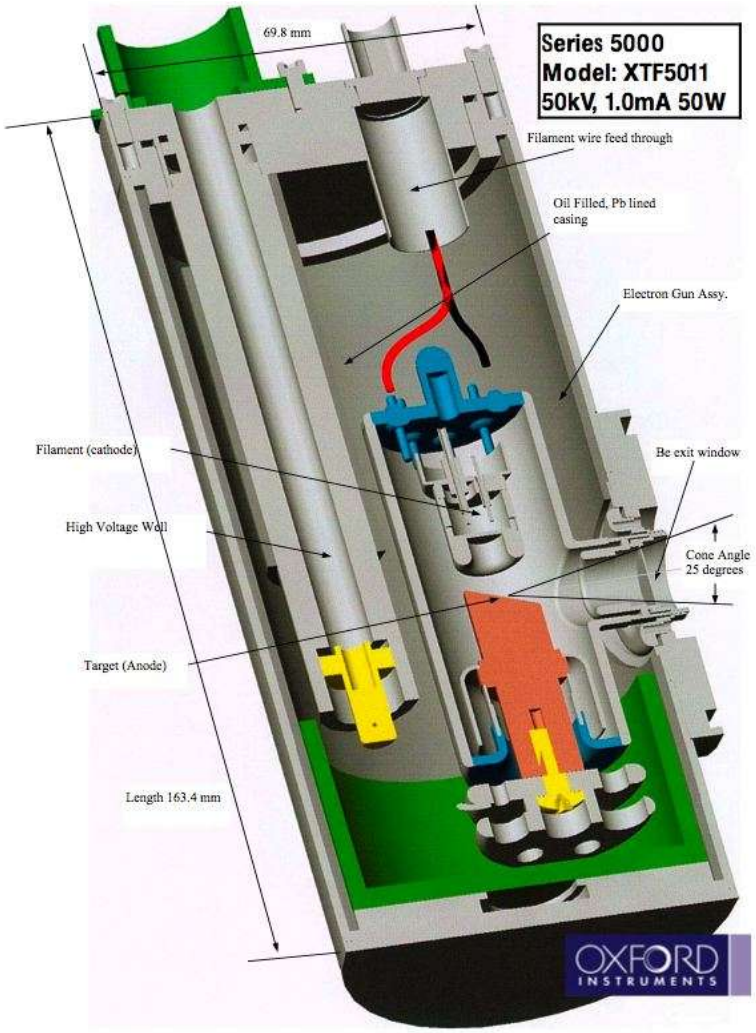

Figure 4: Cross-sectional view of an Oxford X-Ray tube[9], the design of this tube is similar to that used on the bench-top unit

Other mitigation tactics beyond monitoring were considered. However, these alternatives involved installing an intermediary beryllium window between the X-Ray tube exit port and the chamber. This additional window would not only attenuate the X-Ray beam, but more importantly, would increase the amount of beryllium within the system which is undesirable because of the safety issues associated with this toxic metal.

5.4. X-Ray Detector Safety Assessment and Modifications

There are several failure scenarios of the detector, such as mechanical damage or overheating. The detector used is the Amptek[10] XR-100CR which uses a thermoelectrically cooled Si-PIN diode as the X-Ray detector. Modifications were made to lessen the probability that the detector would not be subject to excessive thermal excursions or direct coupling with the electromagnetic field associated with the induction coil. A brass sheath was installed around the detector shaft. This brass sheath provides a conduction path upwards to the cooler portion of the sheath located outside of the chamber, isolates the detector shaft from direct contact with the warm helium within the chamber, and provides susception of electromagnetic fields within the brass rather than the sensitive conducting components of the detector and circuit board.

The tube design consists of a ¾" brass pipe (1.0" OD X 0.81" ID) that is fitted with a press-fitted insert at the bottom and a standard tube compression fitting at the top. The lower insert contains a coaxial outer brass tube and inner aluminum piece that has a conical hole machined along its centerline. This conical hole allows passage of the XRF beam from the molten aluminum target to the detector. The detector is inserted into the brass tube through the tube compression fitting from the top, which is sealed using an o-ring (rather than a ferrule). The resulting assembly was mounted on the chamber using an o-ring sealed vacuum compression fitting as shown in Figure 5. During the initial test of the detector sheath, it was observed that the chamber pump-down to vacuum took a longer time than normal and the pressure was higher at steady-state. However, the associated leak was eliminated by applying a vacuum sealant to the upper tubular compression fitting. The significance of any residual leakage is minor given that during XRF operation the chamber runs at a pressure only slightly less than atmospheric.

Figure 5: View of the brass detector sleeve inserted into the bench-top unit via a vacuum compression fitting.

5.5.Programmable Logic Controller

The programmable logic controller (PLC) is the controller for the IA unit; X-Rays are controlled separately although the PLC interlocks the shutters for the X-Ray tube and sight-glass ports to prevent X-Ray exposure to the user. A view of the configuration of the PLC home screen is shown in Figure 6.

Figure 6: Upgraded PLC for IA Unit

Each number in Figure 6 corresponds to an after delivery custom modification to the PLC that were made to increase the functionality of user control beyond that of the standard user interface. The modifications are listed below.

1. "Stop Pump/Start Pump"- this allows the user to stop the mechanical pump manually at any time. This button will override the program. This was added after it was shown that the vibration of the mechanical pump could cause peak broadening. Additionally, it is not necessary for the mechanical pump to be on when the chamber is at atmospheric pressure anyway and so turning the mechanical pump off has no effect on the quality of the atmosphere after it has been purged with helium.
2. "Stop Heat/Start Heat"- this allows the user to stop the heat at any time. Although the program will continue to display set points, no heating will occur. This is necessary for acquiring data as the heat source interferes with the detector signal. The exact cause of interference is not known but it is hypothesized that the interference is caused by the electromagnetic field associated with the induction coil.
3. "Pause/Resume"- this allows the user to suspend time in the current step of the program while maintaining the current pressure and heat set points. Heating and pumping can also be suspended by pressing "Stop Heat" or "Stop Pump" before the "Pause" button. In case of an unforeseen event that could delay time, this allows the user to overwrite the timer in the current program.

4. “Sample” – the user is able to enter a numeric Sample ID which is recorded in the data output of the PLC.
5. “Temp”- the water temperature of the closed loop glycol cooling water is displayed on the main screen so that any temperature fluctuations can be monitored. It was shown previously that detector temperature changes with fluctuations in cooling water.
6. “Re-Start Diff”- The PLC was reprogrammed so that after the initial pump down, the diffusion pump automatically cools over a period of 10 minutes. This upgrade was done to save time during the shutdown process. However, if the user would like to perform more than one run in a day, this button allows the user to restart the diffusion pump at any point during the cycle.
7. “F”- the user is able to switch between Fahrenheit and Celsius display.

These changes and updates to the PLC have increased the ease of use for all users.

5.6. Optimum XRF Geometry and Settings for Data Acquisition

The optimum XRF geometry and power settings were determined through experimentation. EDXRF systems are count-rate limited and so a setting should be chosen which will excite all elements and will not overwhelm the detector with photons causing excessive dead time. The optimal settings for the 75W tube (50kV and 1.5mA) were a voltage setting of 30kV 1.5mA to provide the maximum count-rate without excessive dead time. The optimum sample height was found to be at 0.65in using a graphite crucible and sample height of 1.192 inches.

5.7.Thermal Profile of Liquid Aluminum Sample

It was important to identify how the melt was solidifying in the graphite crucible out of concern that directional solidification could cause zone refining and increase or decrease solute concentration at the surface of the melt. A thermal survey of the melt was performed at the bottom, mid-height, and surface of the melt and is shown in Figure 7. It was concluded from the thermal survey that the melt was solidifying from top to bottom and the microstructure of the sample supported this conclusion. Therefore, rejected solute interfering with the XRF spectra was not a concern.

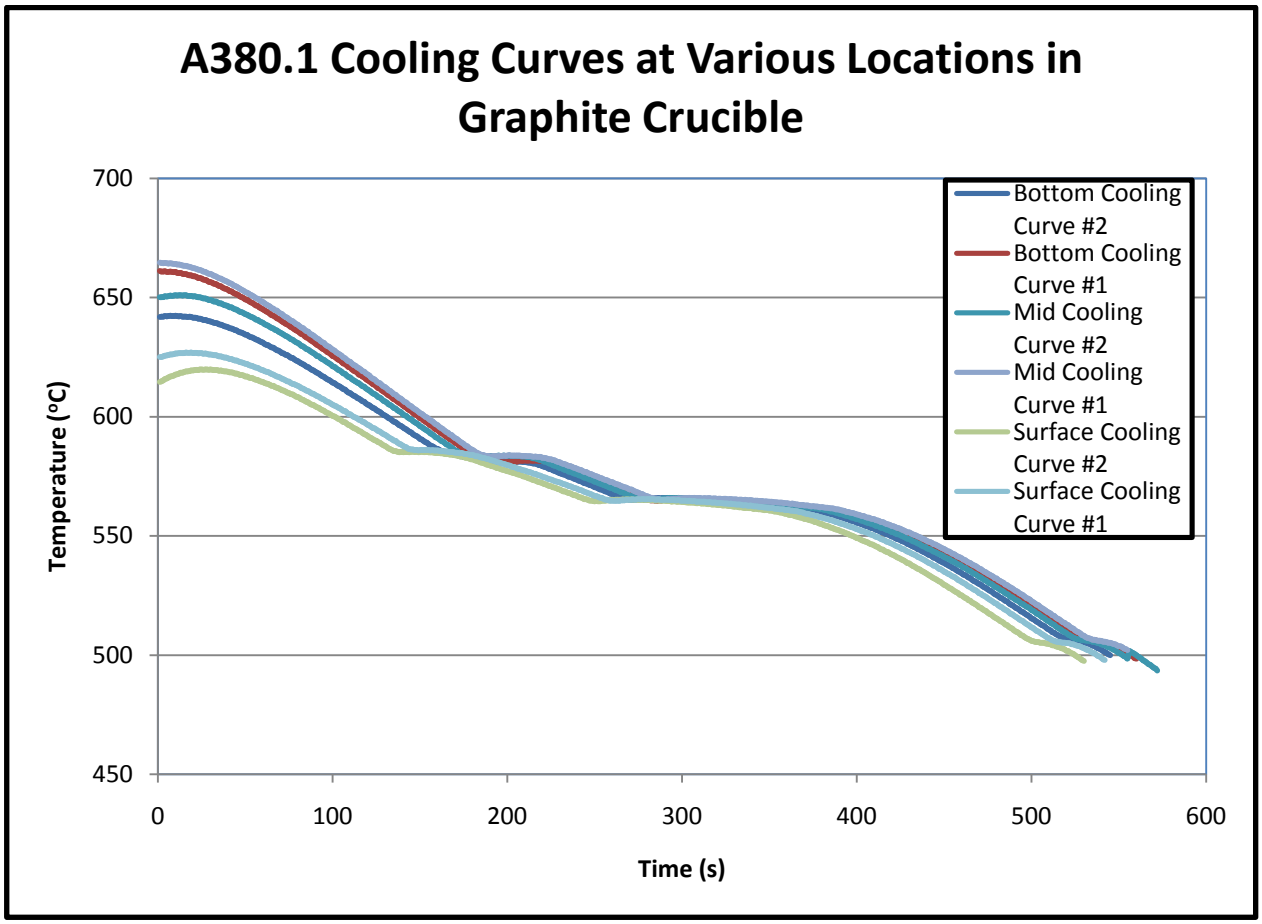

Figure 7: Cooling curves for thermal profile of melt in chamber

5.8.Spectra Analysis

A MatLab routine was written to analyze the peaks of interest in the X38X.X matrix: Al, Si, Fe, Cu, and Zn. The process of the MatLab routine for spectra analysis is first presented in a flow chart form to give the reader a picture of the overall process, Figure 8. A narration of the steps and figures from the MatLab routine are given after the flow chart.

Figure 8: Flow chart of MatLab data analysis process

The peaks of interest are the four major alloying elements and aluminum: Al-Kα (E=1.487keV), Si-Kα (E=1.470keV), Fe-Kα (E=6.403keV), Cu-Kα (E=8.047), Zn-Kα (E=8.638keV) and Cu-Kβ (E=8.904keV). The Cu-Kβ peak was important because it overlaps the Zn-Kα peak.

After the spectrum is imported to MatLab as an array, the user is given the choice to select the peaks of interest. A single peak is shown in Figure 9 and a double peak is shown in Figure 11. The Fe-Kα and Cu-Kα peaks do not overlap other peaks while the Al-Kα and Si-Kα peaks and Zn-Kα and Cu-Kβ peaks do overlap and require and additional parameters within the optimization scheme to successfully fit the double-normal curve shape. The following figures are used to demonstrate the process of the MatLab routine and were generated during analysis of the HHH sample.

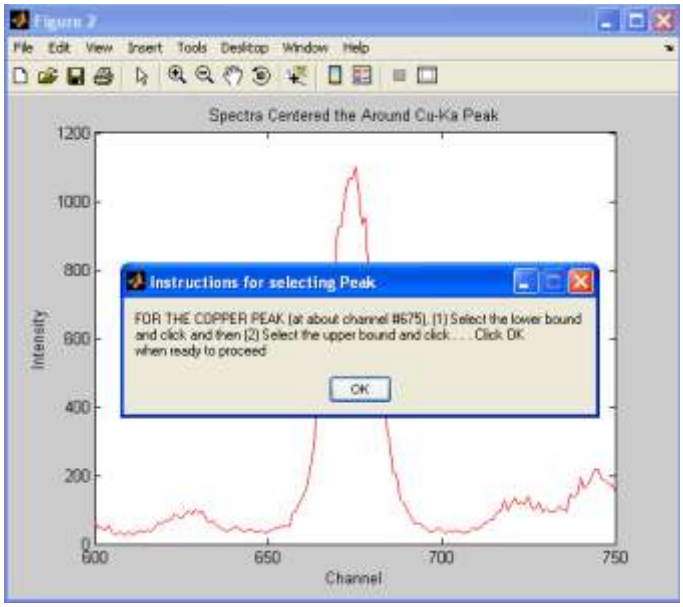

Figure 9: Peak fitting instructions for the Cu-Ka Peak

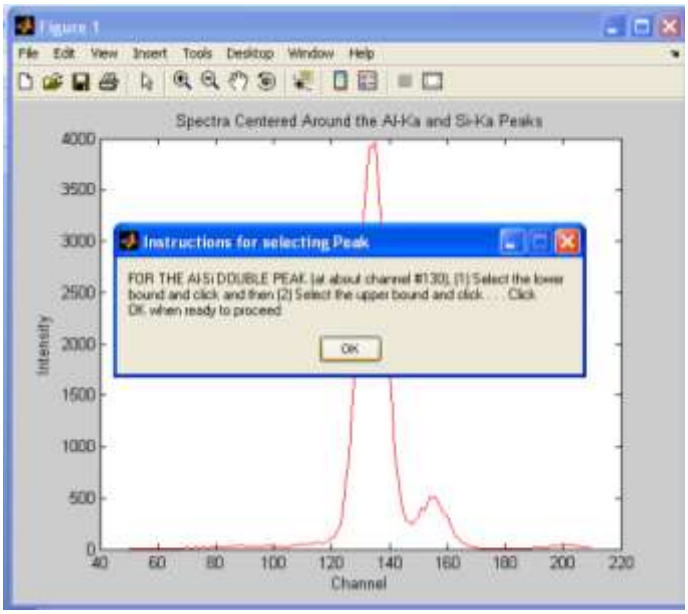

Figure 10: Peak fitting instructions for the Al-Kα and Si-Kα overlapping peaks

After the channels for lower bound and upper bound are selected for the single peaks, the program searches ±20 channels in order to find the best fit which includes a normal fit of the peak and a linear background fit. These channels selected are stored to be used in for future selections of spectra for the same sample. A visual of the chosen fit is displayed for the single peak fit, as shown in Figure 11. Notice that the calibration from channel to energy has not been performed yet.

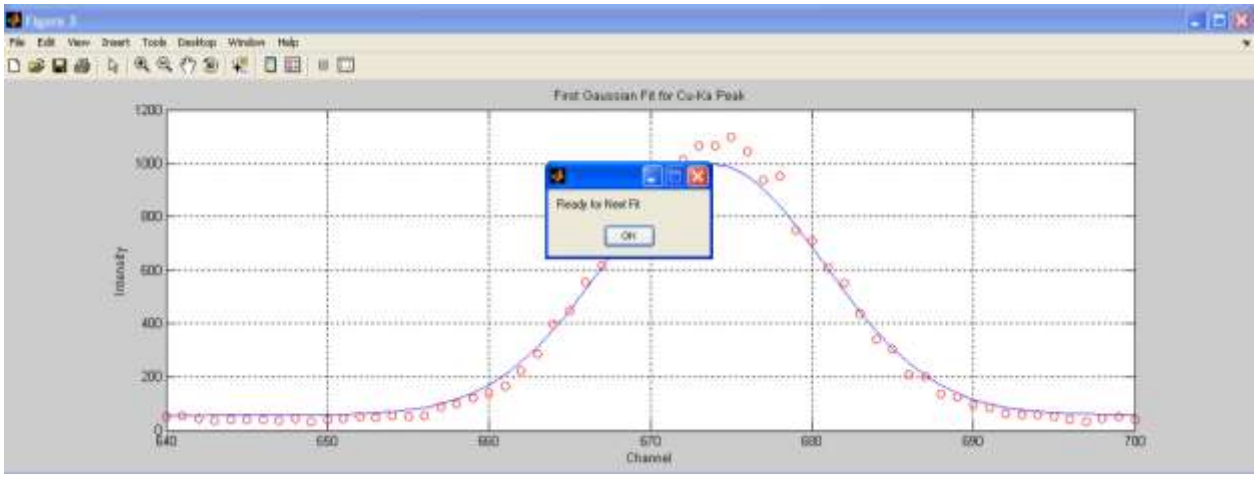

Figure 11: First fit attempt for Cu-Kα peak

For double peaks the user must select addition parameters as starting points for the program to search for peaks. The user selects the peak height of each peak as well as the as well as the width at half peak height. In this case, a linear background and two normal distributions are fit to the peaks as shown in Figure 12. Note that the manually selected parameters provide starting values and bounds for the optimization routine that selects the best set of curve parameters in a least squares sense.

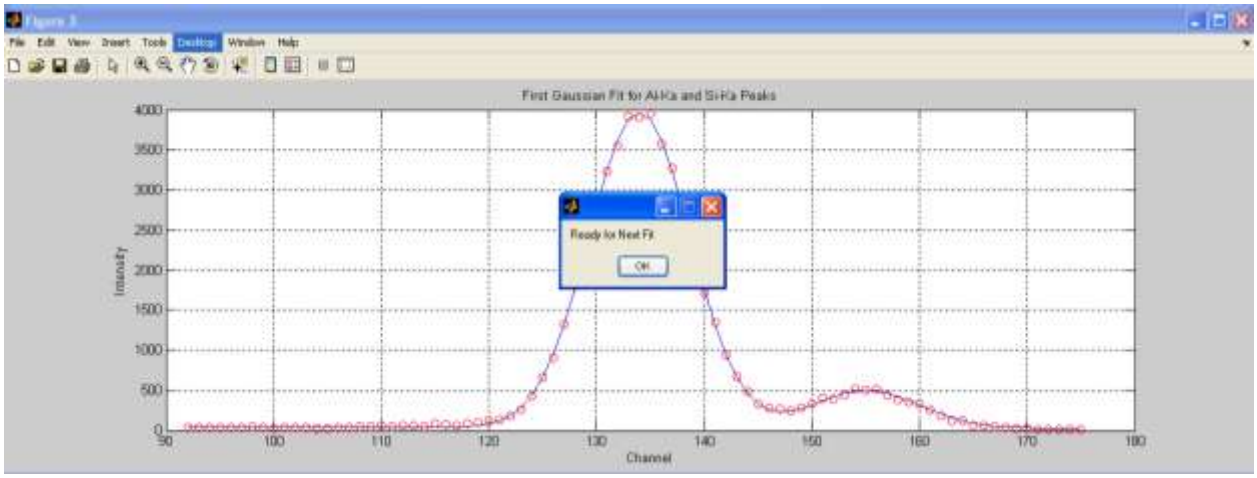

Figure 12: First fit attempt for Al-Kα and Si-Kα double peak

After the first fits have been made to the peaks of interest a graph is shown that represents the percent deviation of the known energy of the peak to that of the non-linear calibration curve where Al-Kα, Si-Kα, and Fe-Kα are forced by the non-linear calibration curve to have a zero-percent deviation

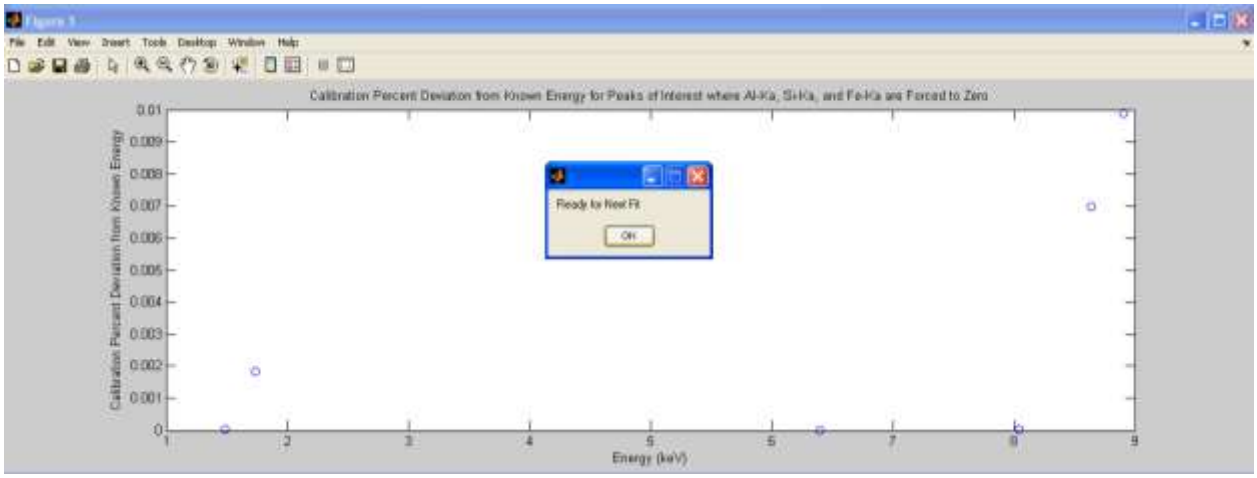

Next the peaks are refit and optimized using the energy scale on the x-axis. The refit does not require any new selections by the user but graphical displays of each are shown so that the user can visually inspect the fit of the data. The final normal fit curves are shown in and for the Cu-Kα fit and the Al-Kα/Si-Kα fit in Figure 13 and Figure 14 respectively.

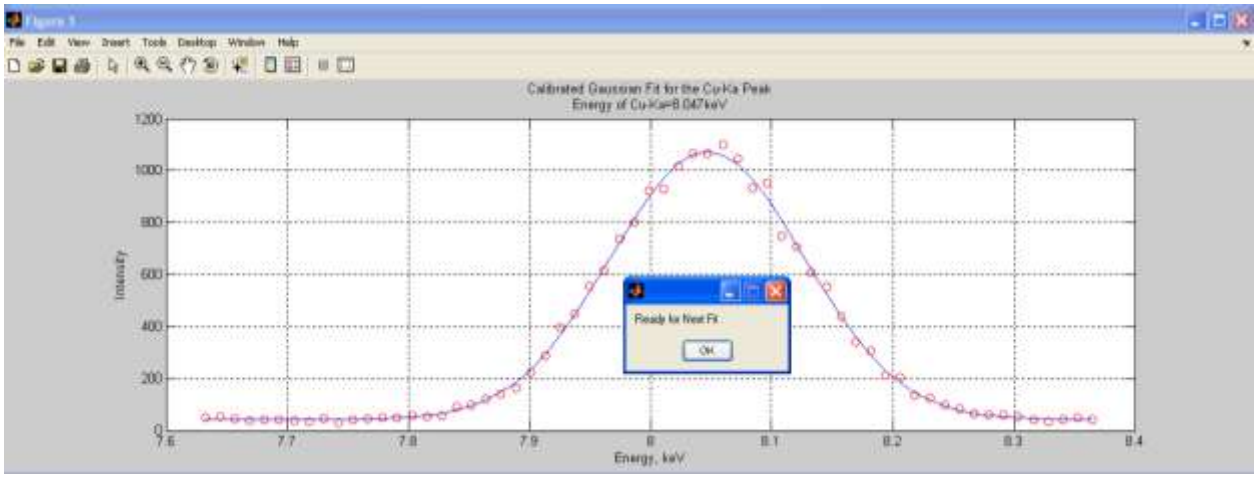

Figure 13: Final normal fit and background subtraction of the Cu-Kα Peak

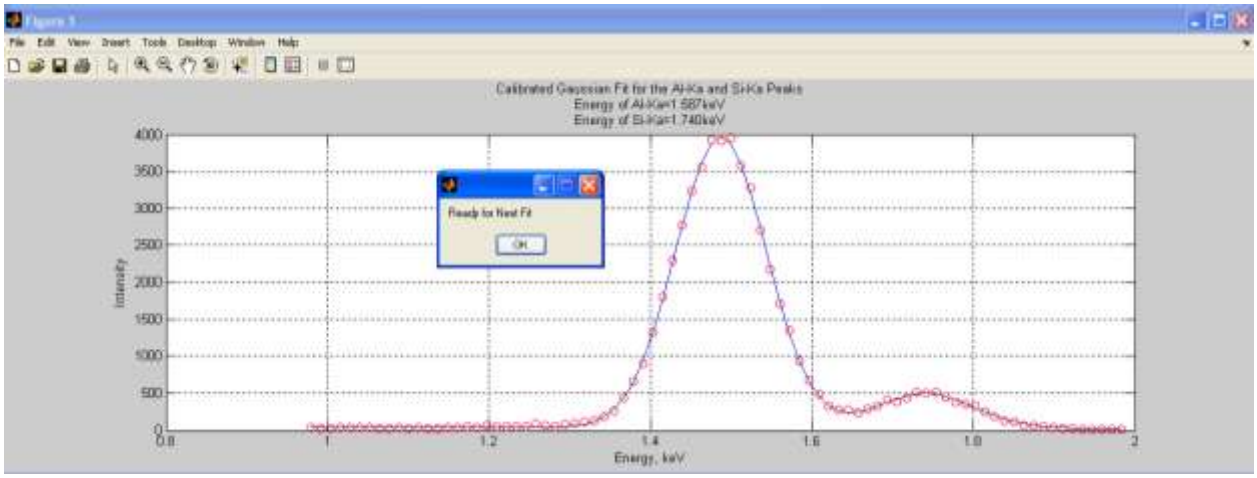

Figure 14: Final normal fit and background subtraction of the Al-Kα and Si-Kα double peak

Lastly, a text file is created that holds the metrics used to evaluate the spectra. The spectra metrics computed are: the peak height of the actual data minus the calculated background, the peak height of the normal fit minus the background, the area under the peak minus the background, the area under the actual data from the calculated full width at half maximum minus the background, the area under the fit peak from the calculated full width at half maximum minus the background, and the full width at half maximum. The area under the fitted peak best represents the total count of characteristic energies for each element and was used for the relationship between intensity to concentration.

5.9. Repeatability of XRF Spectra

A repeatability study was performed to determine the repeatability of the XRF system. Twenty spectra were taken for an MMM sample in the solid state with optimum XRF settings and a 30s data acquisition time, with approximately 15s in between each acquisition. The chamber was filled with helium and the oxygen sensor typically read 0 ppm during measurements; it was never above 1 ppm.

Before the spectra were analyzed, the raw, unanalyzed intensity of the aluminum peak was compared to determine if there was a trend in the data as a function of trial number. Figure 15 shows that there is a decrease in aluminum peak height with intensity as the trial number increases. To correct for this all samples were normalized to the number of overall counts in the first trial.

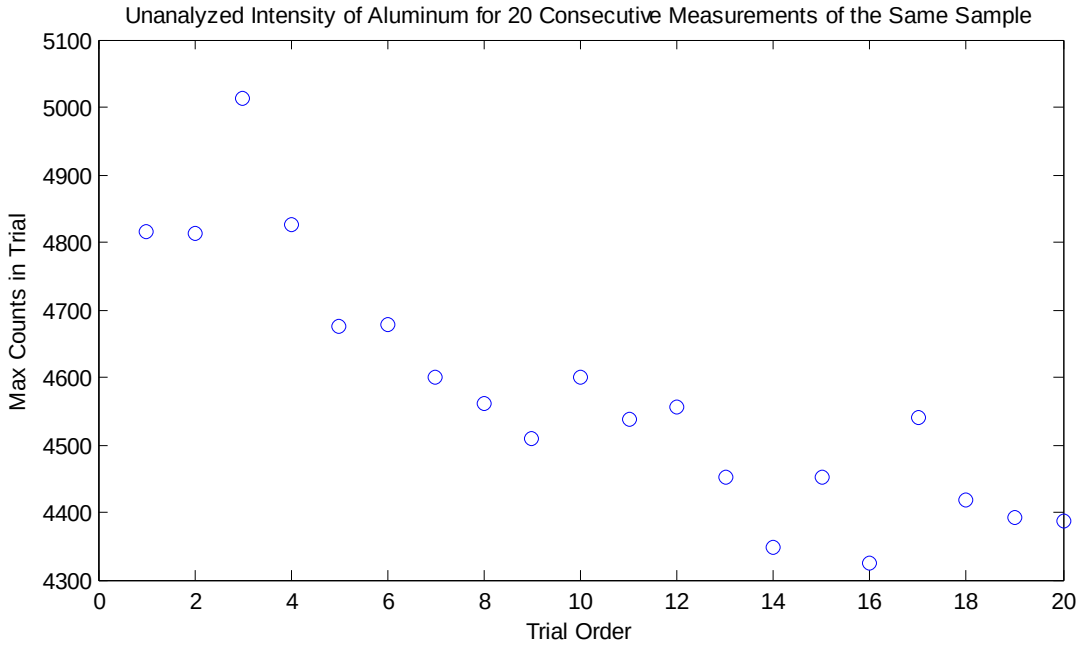

Figure 15: Unanalyzed Intensity of Aluminum Peak for 20 Consecutive Measurements of the Same Sample

Each spectrum was analyzed using the MatLab program and the same channels were used for analysis after they were manually picked for the first spectra. Two metrics were used to determine the normality of the spectra: "Area Under the Curve" and the "Fit Height" for each peak. The data was analyzed using the MatLab "normplot" function which plots a normal probability plot of the data and superimposes a line on the plot joining and first and third quartiles of the data. The purpose of the plot is to graphically assess whether the extracted metrics follows a normal distribution. The results for the aluminum characteristic emission energy are located in Figure 16 and Figure 17 respectively. The rest of the data follows a similar normal distribution and can be found in Appendix C: Probability Plots for Repeatability of Spectra.

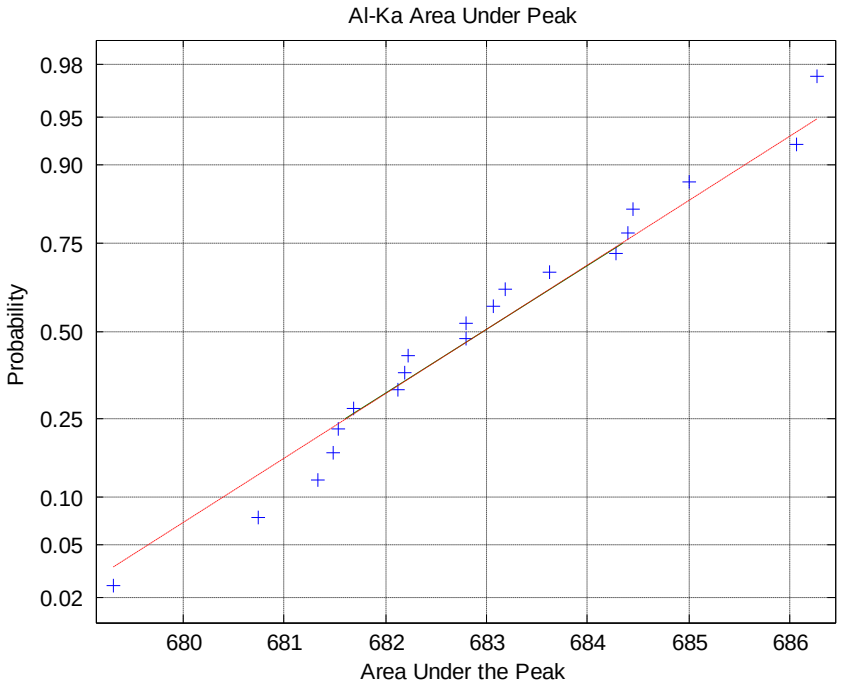

Figure 16: Normal probability plot for the area under the Al-Ka Peak for 20 Consecutive Trials

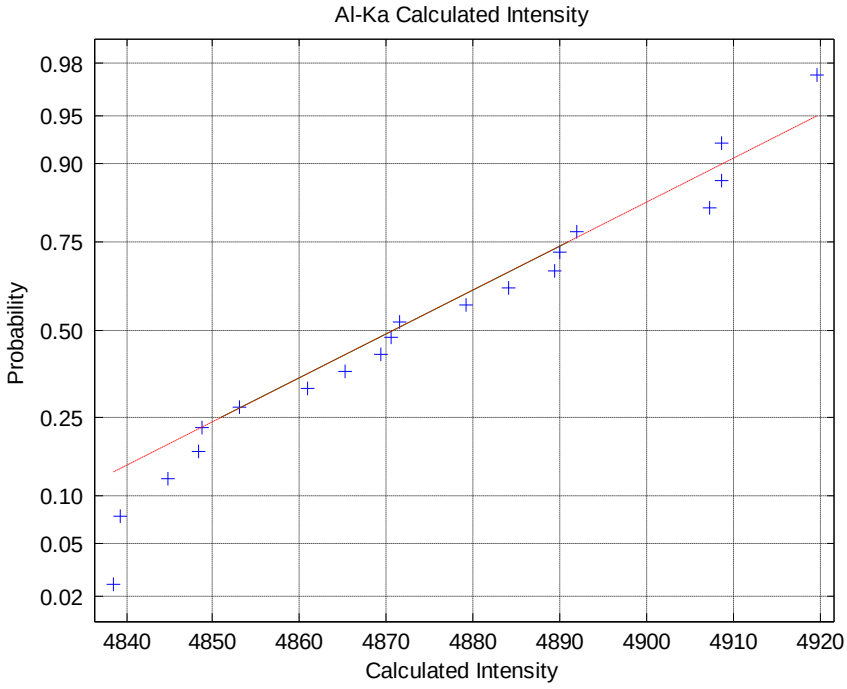

Figure 17: Normal probability plot of calculated intensity for Al-Ka

Slight deviations from the normal trend (particularly in the tails) can be attributed to the low sampling population (n=20) and it is likely that if more trials were performed the fit to the normal curve would increase.

5.10. Effect of Data Acquisition Time on Spectra Metrics

The same twenty spectra used in the repeatability of XRF spectra were used to determine the effect of data acquisition time on the spectra metrics presented in the data analysis section. Spectra were added together to obtain representative spectra for data acquisition times of 30s, 1min, 2mins, 2.5mins, 3mins and 5mins. A small data acquisition time is desirable to users, but a large sampling time decreases uncertainty due to counting statistics. The fit peak heights were normalized to that of aluminum to determine if the spectra provided sufficient data to discriminate all peaks of interest from background. The results are presented in Table 5. Notice that the ratios are consistent to the fourth decimal place, and inconsistencies show no trend.

Table 5: Effect of data acquisition time on spectra metrics

Ratio of Peak Heights to Al-Ka for Varying Data Acquisition Times						
	0.5min	**1min**	**2min**	**2.5min**	**3min**	**5min**
Si-Ka	0.1421	0.1422	0.1423	0.1423	0.1422	0.1423
Fe-Ka	0.0830	0.0830	0.0830	0.0830	0.0830	0.0831
Cu-Ka	0.2445	0.2447	0.2446	0.2447	0.2444	0.2446
Zn-Ka	0.0169	0.0169	0.0169	0.0169	0.0169	0.0168
Cu-Kb	0.0423	0.0423	0.0423	0.0423	0.0422	0.0424

Based on the results in Table 5, it was concluded that the spectra provided sufficient counts for all data acquisition times based on the standard deviation of the normal fit for each peak; background could be discriminated from peak area in all cases.

5.11. Effect of Sample Height Due to Melting

Consistent geometry is very important for accurate quantitative analysis of XRF spectra. JMatPro software was used to calculate the molar volume of each alloy as a function of temperature to determine the height of sample before and after melting. All samples were machined to a uniform height so that initial XRF in the solid state was performed at a uniform height for all samples. To simulate the effect of height due to melting, solid spectra were taken at four heights: solid height of all samples, liquid height of LLL, liquid height of MMM, and liquid height of HHH. The heights were determined based on the molar volume predictions from JMatPro and it was assumed that the surface of the melt was flat. The maximum difference between in height was between the solid height and the HHH sample, a difference of -0.14in from the position of the solid sample. The results of the XRF spectra are shown below in Figure 18 and Figure 19.

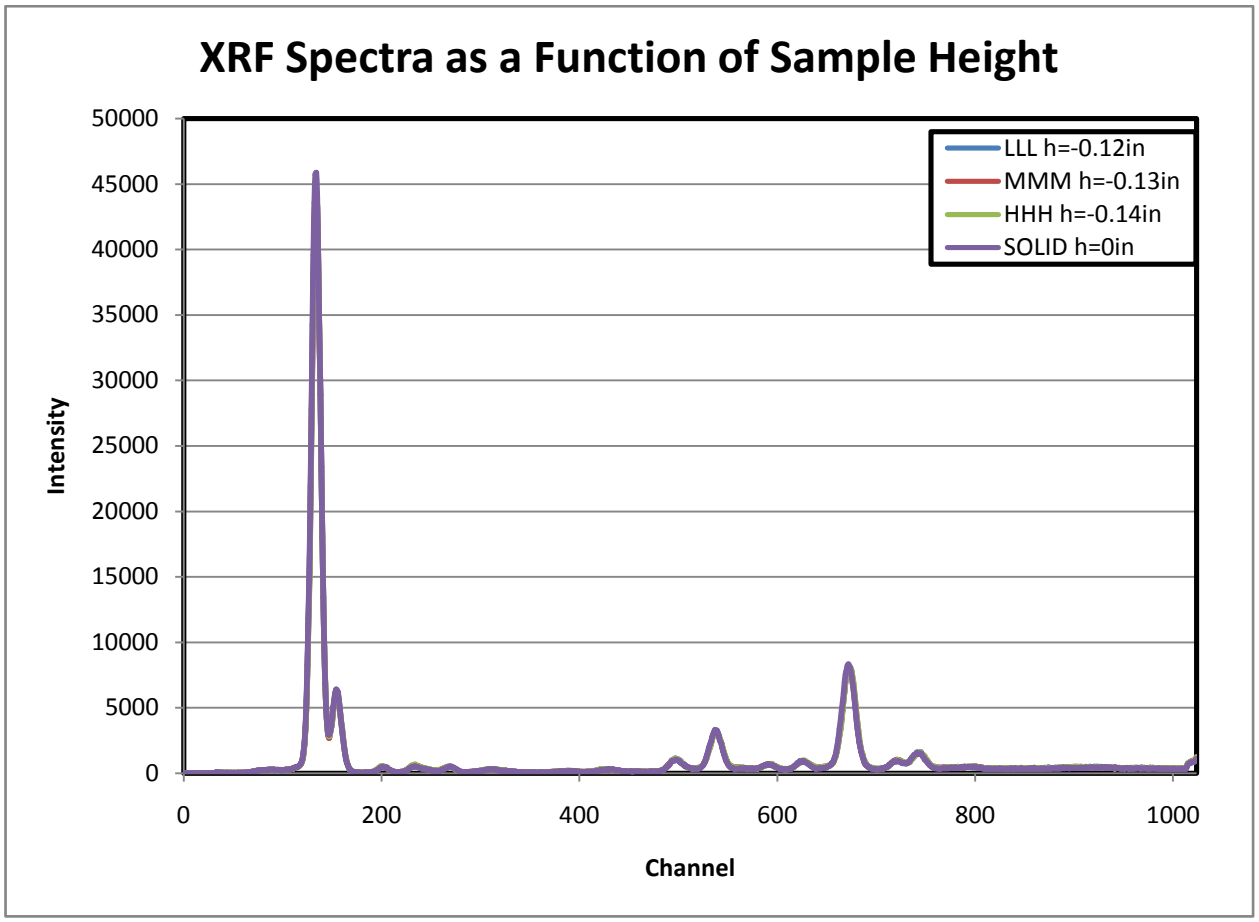

Figure 18: XRF Spectra as a Function of Sample Height

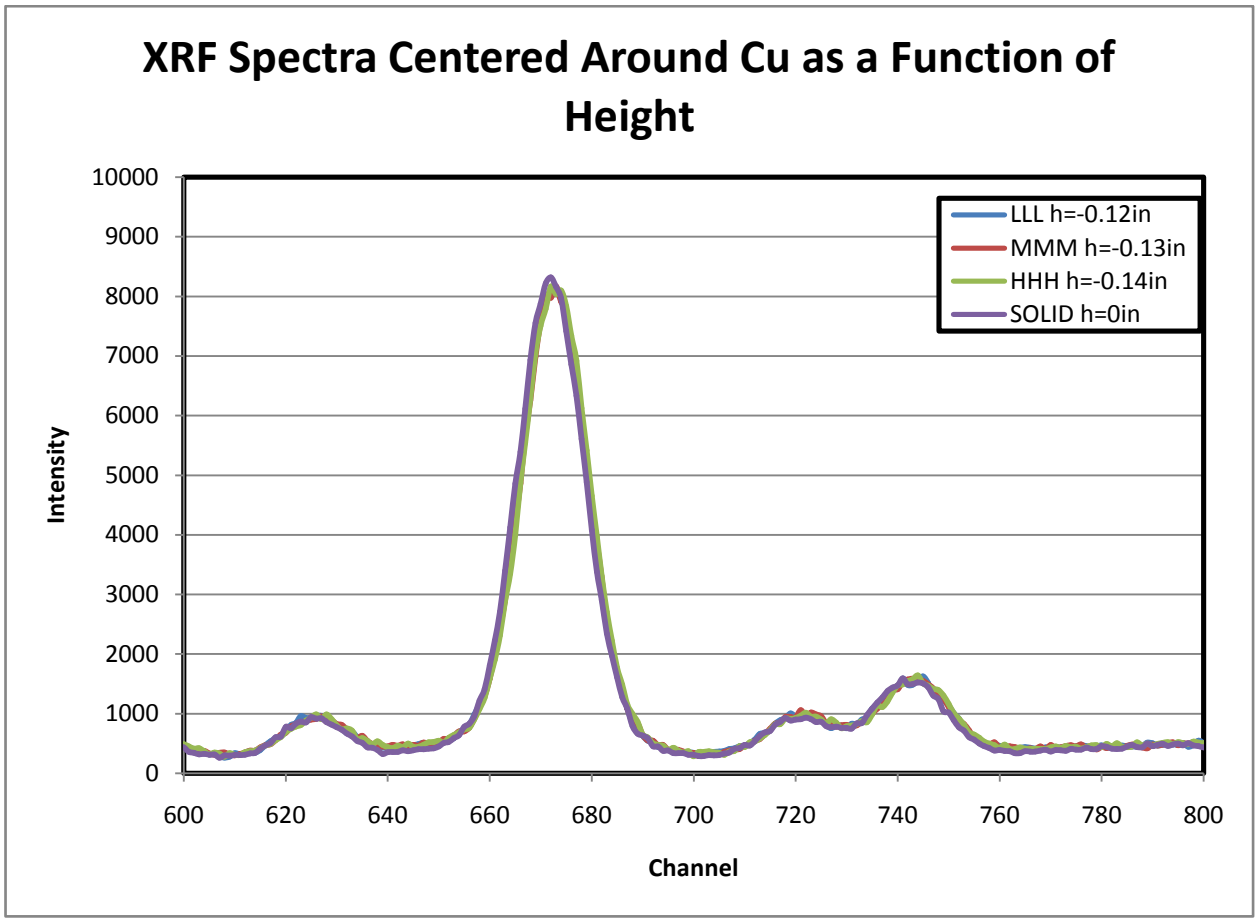

Figure 19: XRF Spectra of Cu as a Function of sample height

Visual inspection of the spectra does not show any more variation than the variation between spectra taken in the repeatability tests. Therefore, adjustments in sample height were not made before and after melting because the spectra did now show any significant changes, other than minor differences attributed to counting statistics, for height differences that correspond to those calculated for the liquid level of the LLL, MMM, and HHH.

5.12. Analysis of Liquid XRF Spectra

The liquid spectra were analyzed according to the MatLab protocol. For each sample, the same channels were used for peak selections, but between samples channels were chosen by the user because there is variation in peak location between samples. In total, six samples were analyzed: two each of LLL, MMM, and HHH. Two liquid spectra were taken per sample along with a spectrum in the solid state before melting and after melting. The results are presented for the Kα line of each element of interest (Si, Fe, Cu, and Zn). Although the Cu-Kβ spectra metrics were calculated, only the Cu-Kα results are presented as the Cu-Kα line is much stronger. All of the data presented in this section was taken in the liquid state. The data is presented as the ratio of the peak area for the element of interest to the peak area of the Al peak in order to be able to make meaningful comparisons between spectra.

Because of the electromagnetic interference caused by the induction coils, liquid measurements were not taken isothermally. However, temperature and visual monitoring ensured that the sample was in the liquid state for the duration of the XRF data acquisition. All liquid measurements began at 680±5°C and ended at 620±5°C. Graphs in Figure 20 through Figure 23 present the relationship between peak area and concentration for the four major alloying elements of interest. In all cases, the fit line is forced through zero for a visual representation of the ideal relationship between peak area and concentration to the actual data.

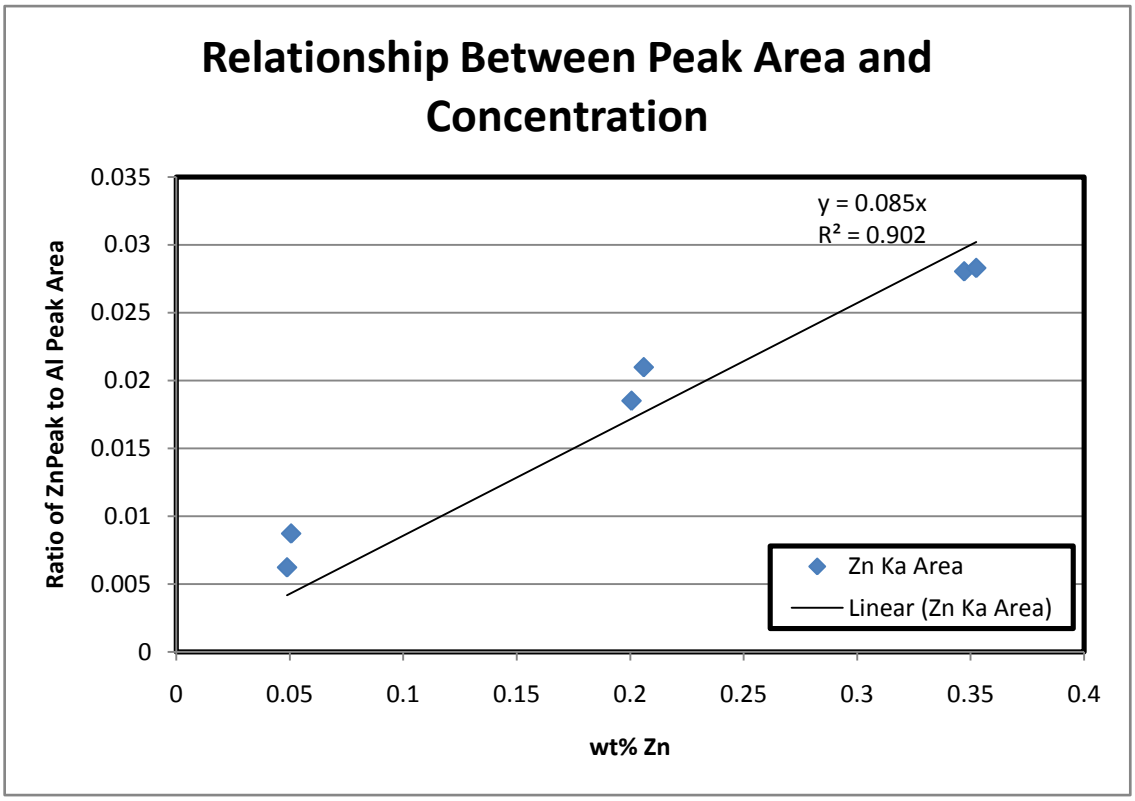

Figure 20: Relationship between peak area and concentration for Zn as a function of weight percent

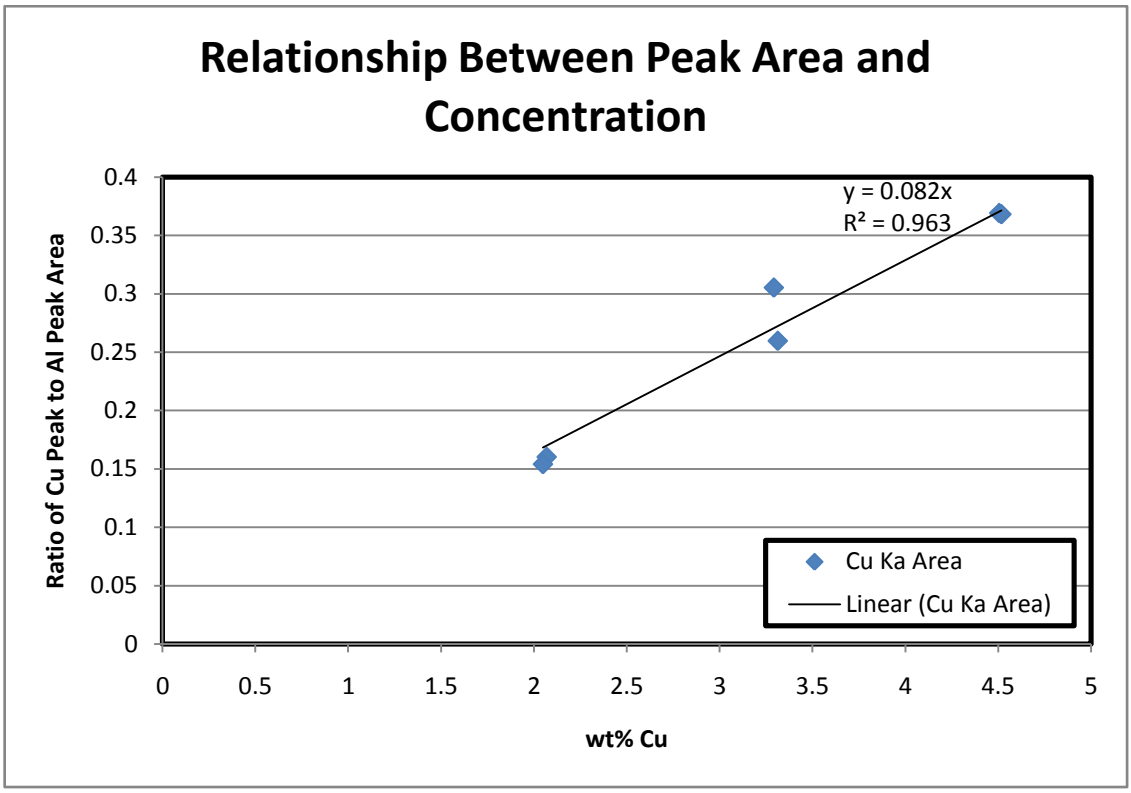

Figure 21: Relationship between peak area and concentration for Cu as a function of weight percent

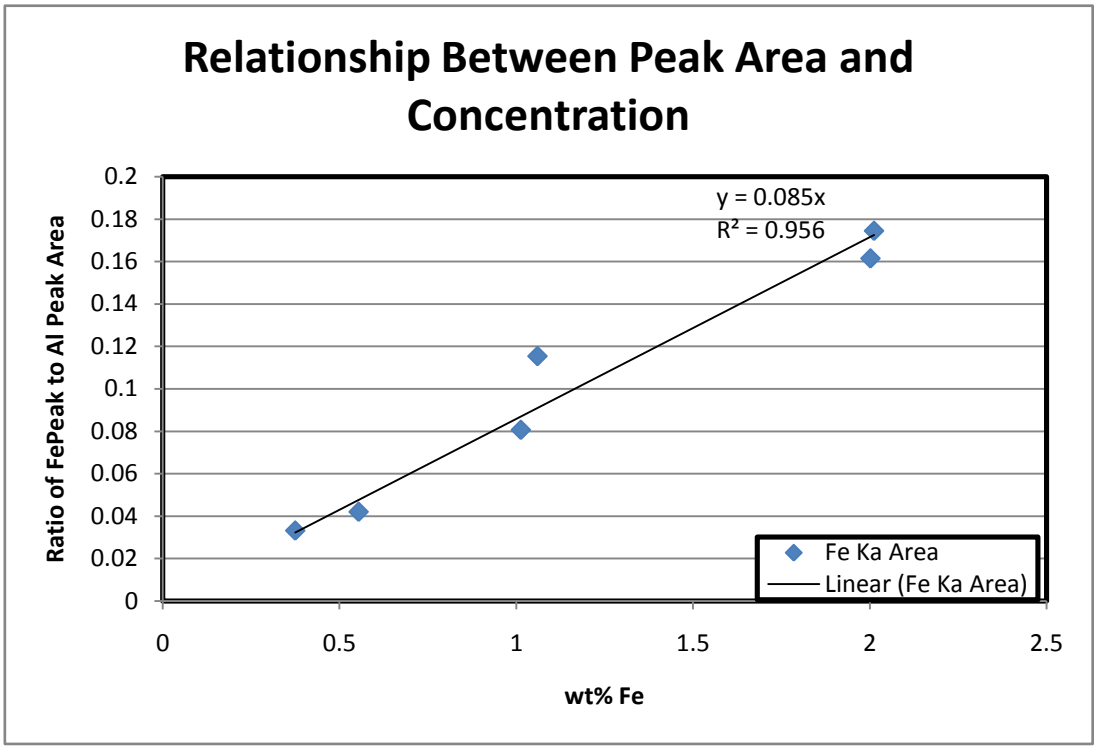

Figure 22: Relationship between peak area and concentration for Cu as a function of weight percent

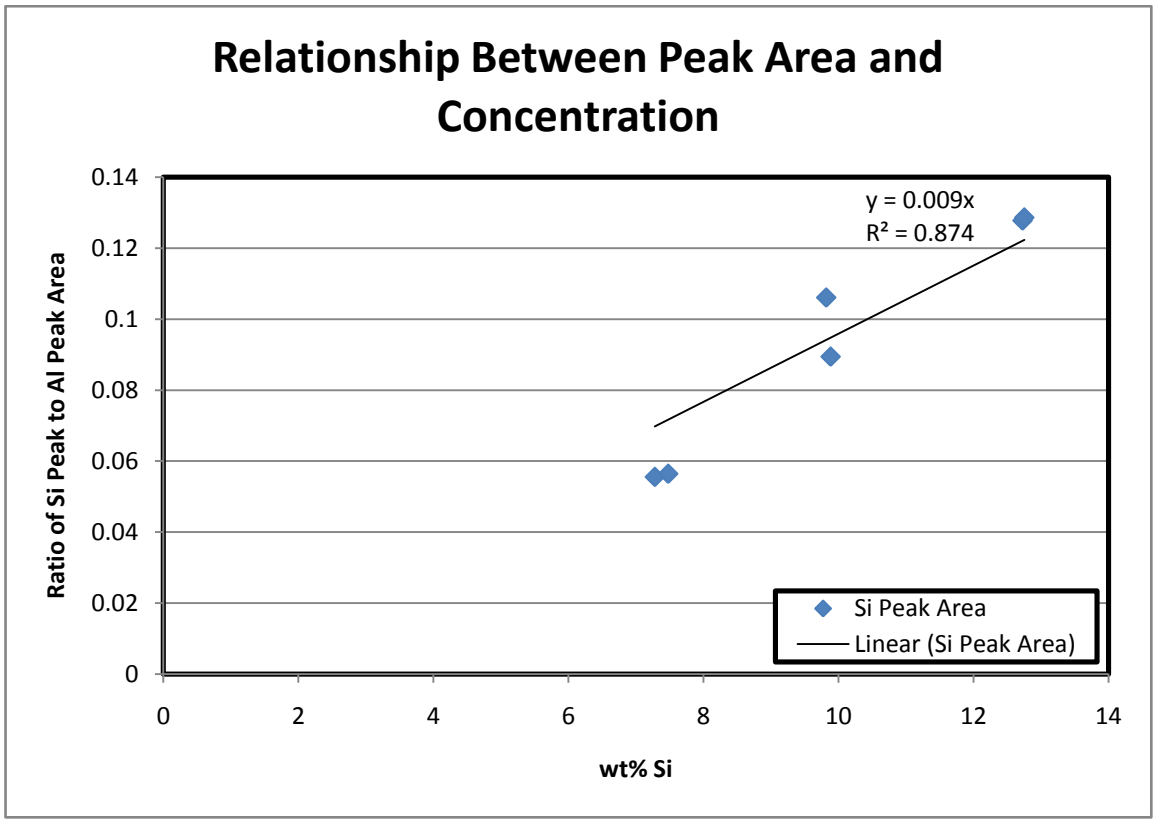

Figure 23: Relationship between peak area and concentration for Si as a function of weight percent

The deviation from a straight line linear relationship can be attributed to the absorption effects as well as enhancement effects. The calculated secondary absorption effects are presented in the next section and can be applied to the fundamental parameters approach.

The fundamental parameters approach which will be used after the completion of testing the entire 2-4 Half Fraction Factorial virtually eliminates the needs for standards and relies on fundamental data such as mass absorption coefficients and fluorescent yields. In the past, this method has been too expensive for most research laboratories but the increased computing power of personal computers has made the method more widely used. The procedure for the fundamental parameters method involves measuring the X-Ray tube spectrum and replacing it in an integral form. The reader is referred to Reference 3 pp. 22-23 and 369 for the details of the integral equation.

5.13. X38X.X Matrix Effects

This section presents the results of secondary absorption matrix effects for the LLL, MMM, and HHH alloys of the X383.X alloy space. Since secondary absorption contributes the most to the matrix effects, only secondary absorption was calculated. The matrix effects of the X38X.X alloy composition were investigated to determine the effect that the change in alloying composition would have for the three alloys of interest, which ultimately has an effect on converting characteristic line intensity into composition.

This work focused on secondary absorption. Secondary absorption is determined by referencing the mass absorption of each element in the matrix as a function of energy. The mass absorption data was obtained from a NIST database[11]. Absorption coefficients for each characteristic emission line were estimated by graphing the data and estimating the intersections of characteristic emission lines and the mass attenuation data. The data is graphed in Figure 24. Additional graphs centered and fit to each characteristic emission line are located in Appendix C: Mass Attenuation for the X38X.X Matrix.

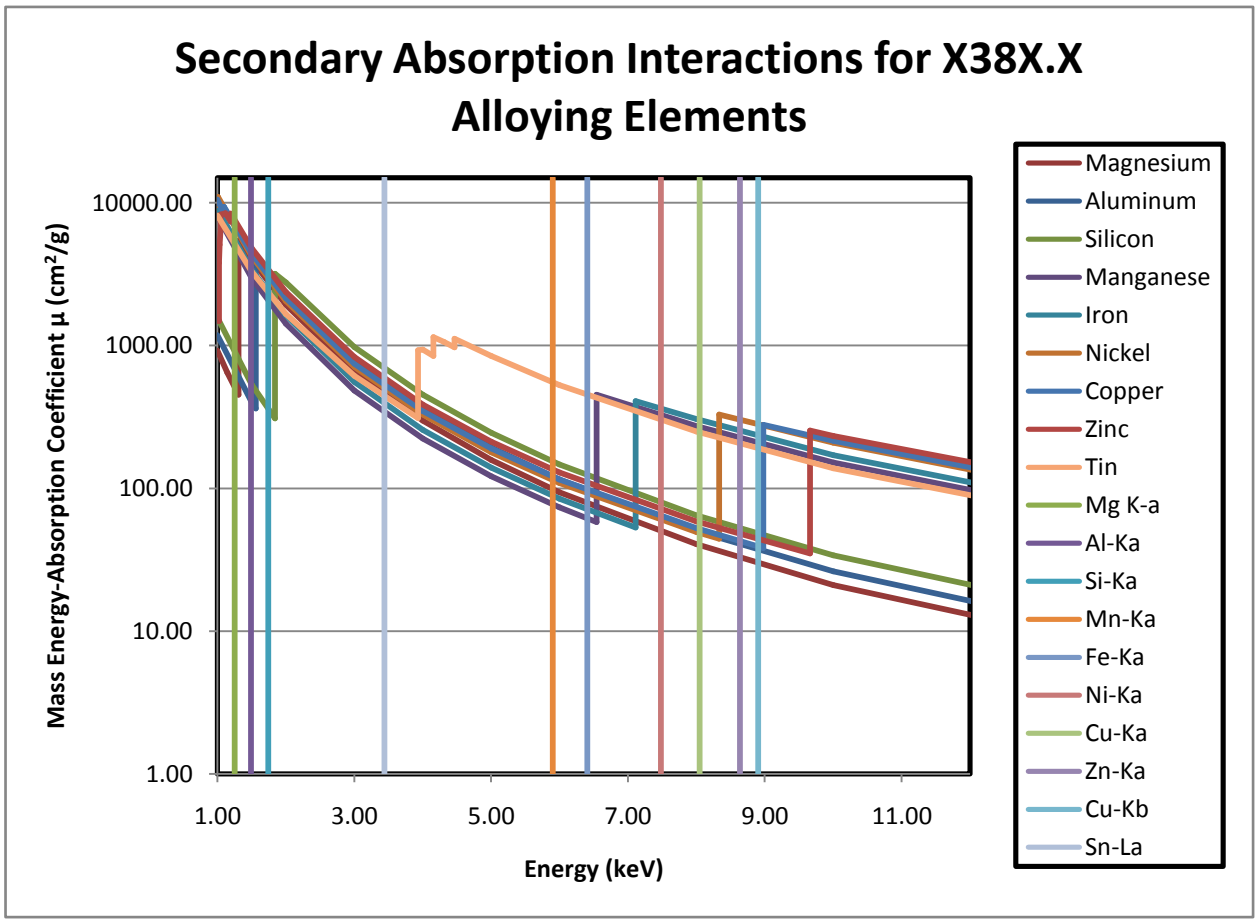

Figure 24: Mass Absorption Interactions for X38X.X Alloying Elements

To calculate values of the mass attenuation coefficient for homogeneous mixtures and compounds simple additivity was used: $\frac{\mu}{\rho} = \sum_i w_i \left(\frac{\mu}{\rho}\right)_i$ [11] where w_i is the weight fraction of the i^{th} atomic constituent and the $\left(\frac{\mu}{\rho}\right)_i$ value is the mass attenuation coefficient for the i^{th}atomic constituent.

The results for secondary absorption effects are shown in Table 6.

Table 6: Secondary absorption matrix effects for the alloys of interest

Matrix Effects for X38X.X Alloying Elements

	wt%			μ (cm^2/g)			% Change		
	LLL	MMM	HHH	LLL	MMM	HHH	LLL	MMM	HHH
Si	7.5	10	13	3040.57	2963.52	2869.20	0	-2.53	-5.64
Fe	0.4	1	2	104.71	105.17	105.66	0	0.45	0.91
Cu	2	3.25	4.5	110.49	112.70	116.00	0	2.01	4.99
Zn	0.05	0.2	0.35	125.40	126.02	126.66	0	0.49	1.00
Mg	0.15	0.15	0.15	1011.13	1140.83	1293.63	0	12.83	27.94
Mn	0.25	0.25	0.25	45.88	47.35	50.59	0	3.21	10.26
Ni	0.25	0.25	0.25	70.33	73.02	77.00	0	3.83	9.49
Sn*	0.2	0.2	0.2	609.21	611.14	613.11	0	0.32	0.64
Al	89.2	84.7	79.3	560.48	638.81	730.36	0	13.98	30.31

***Please note that all effects are calculated for the Ka line, except in the case of Sn where the La line is used.**

Note that this table does not include enhancement effects, only secondary absorption effects, where secondary absorption effects are investigated as a first look at matrix effects. Notice that Si is the only element for which the mass attenuation coefficient is decreasing from the LLL to HHH alloy. This is predicted to have an effect on the calibration curve of negative deviation from linearity which can be observed in Figure 23. This effect can be attributed to the decreasing content of aluminum while all other elements are increasing; not as much aluminum is available to absorb the Si fluorescence.

5.14. Liquid and Solid State Spectra Comparison

In all cases, there were differences similar to those shown in Figure 25 between the liquid and solid state spectra. No quantitative comparisons were made between samples, but hypothesis are made as to why these differences might be occurring. The spectra for a HHH sample is shown in Figure 25 . Four spectra are shown and are labeled accordingly; there are two samples taken in the solid state and two taken in the liquid state. The four spectra were normalized to the same number of total counts.

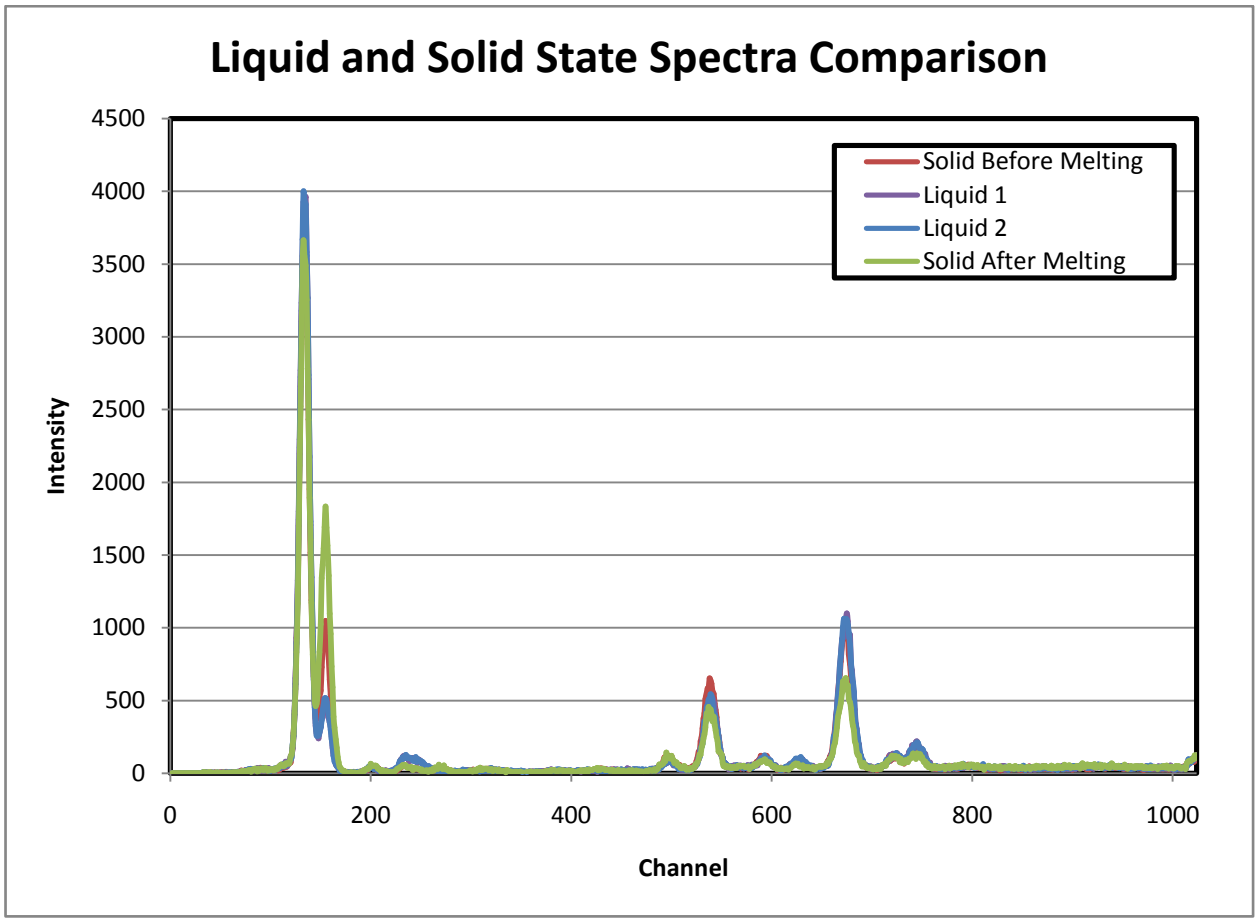

Figure 25: Qualitative liquid and solid spectra comparison of an HHH sample

It should be observed that the silicon intensity, at approximately channel 180, decreases significantly in the liquid state whereas Fe, at approximately channel 550, Cu at approximately 675, and Zn at approximately 720 all increase slightly in the liquid state. The Si and Cu peaks are chosen to demonstrate this effect and are shown in Figure 26 and Figure 27 respectively.

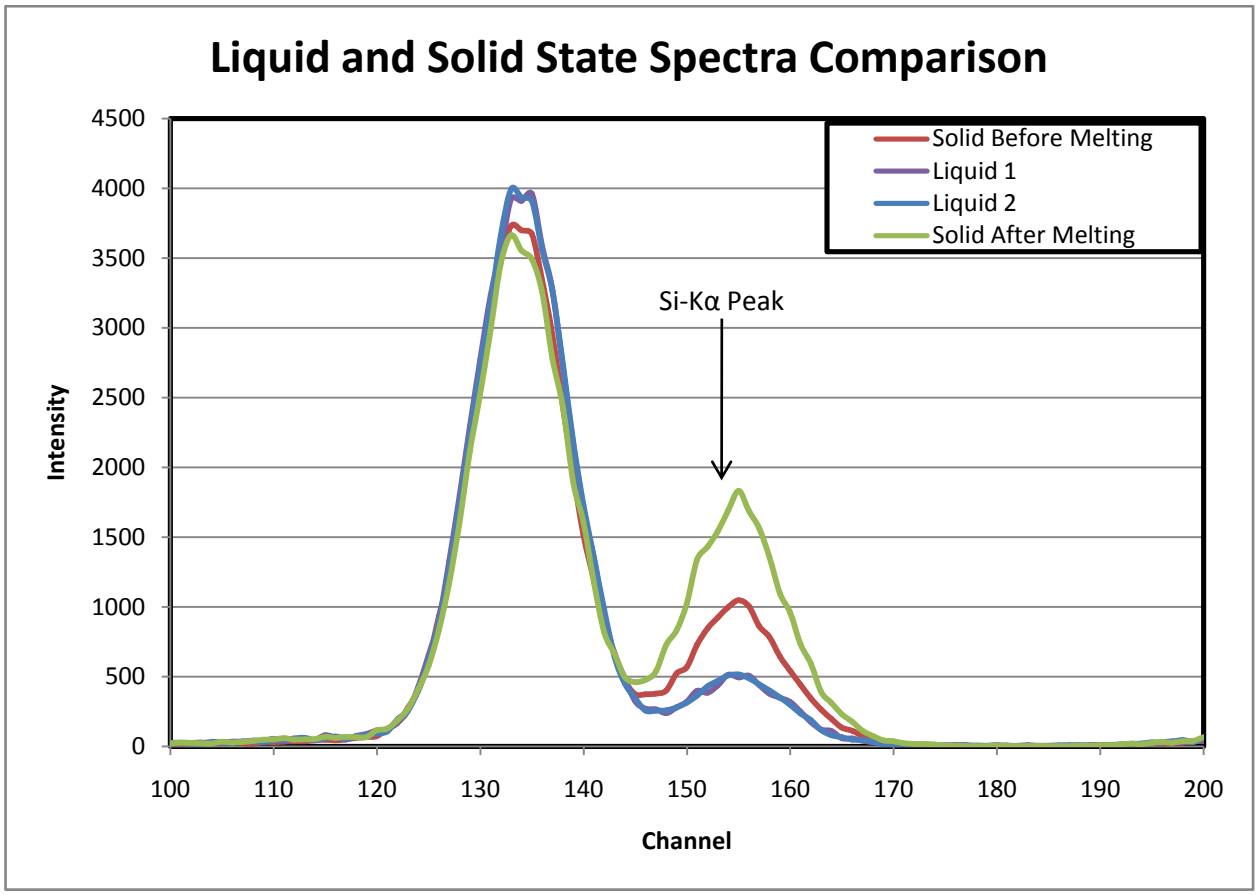

Figure 26: Qualitative liquid and solid state spectra comparison of the Si-Ka Peak

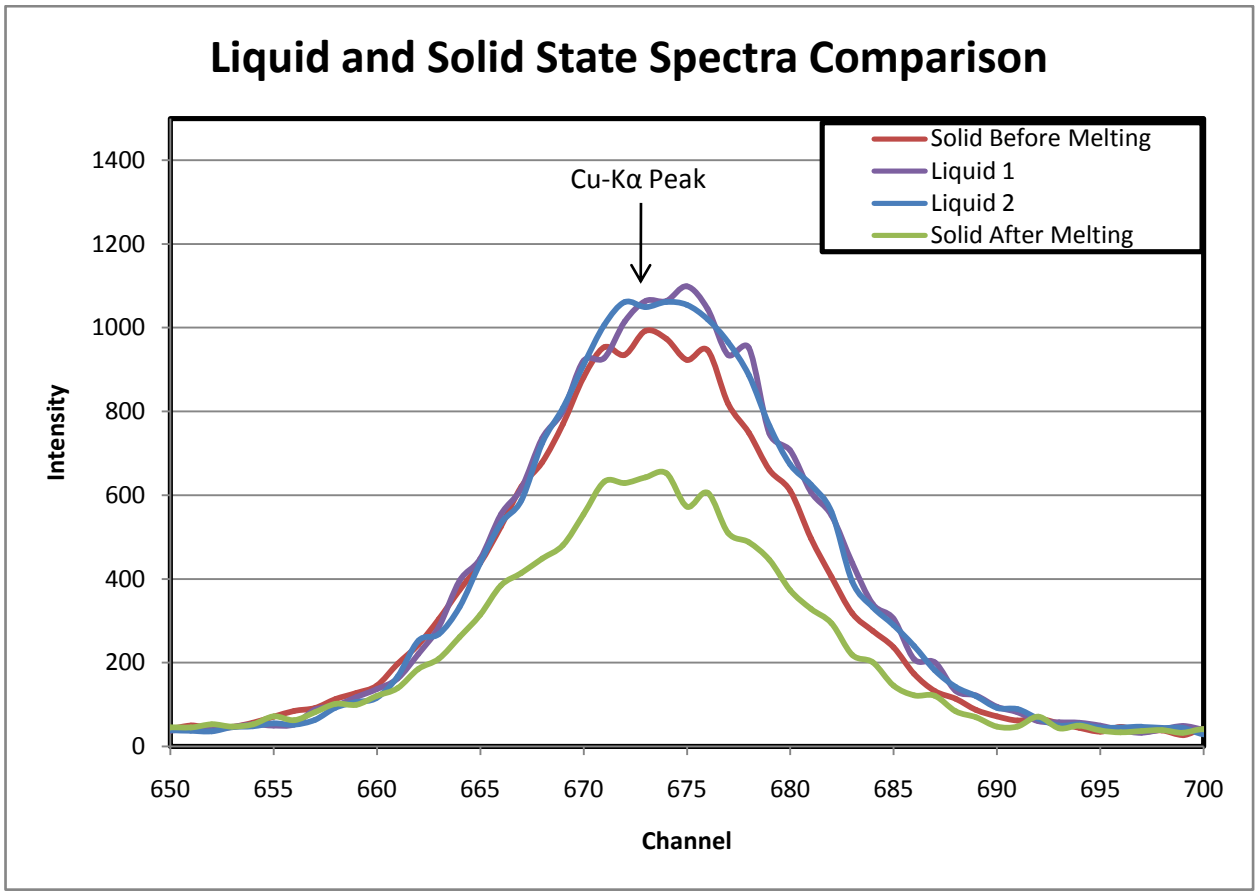

Figure 27: Qualitative liquid and solid state spectra comparison of the Cu-Ka Peak

These spectra show that application of XRF technology will require separate calibration curves for liquid and solid samples. The reason for the changes in spectra is unknown at this point in the program, but several possible explanations have been formulated to explain the nearly 50% decrease in the Si intensity at the liquid state.

It is hypothesized that the relative decrease of Si peak intensity (increase for other element intensities) could be an effect of elemental segregation at the melt surface due their effect on surface tension. According to Gibbs adsorption theory, elements that reduce surface tension will preferentially adsorb on a surface, in effect to reduce surface energy. Park et al.[12] have shown that while Zn and Cu have no effect on the surface tension of liquid Al, Si decreases the surface tension of binary liquid Al-Si. Therefore, silicon should positively segregate at the surface and would tend to increase the XRF intensity of the silicon peak in contradiction to the XRF results. However, precise surface tension measurement of liquid metals is extremely difficult[13] and the effect of silicon on surface tension could be significantly different for the multicomponent alloys used in this research.

A second possible explanation involves the Debye-Waller effect which describes the attenuation of X-Ray scattering caused by atomic thermal motion (phonons) and is applied most notably to explain and correct for the significant effect of temperature on X-Ray diffraction intensities . While temperature diffuse scattering (associated with the Debye-Waller effect) could possibly increase the mean path

length for silicon fluorescent x-rays and thereby increase their probability of absorption by aluminum, this effect is uncertain. Additionally, it is unclear how the Debye-Waller effect can explain the concurrent increase in spectral intensity for the other elements (e.g., copper).

A third explanation could relate to the fact that the initial solidification product (alpha and AlFeSi-beta) are silicon bearing phases that are also denser that the bulk molten alloy, see Figure 28 and Figure 29. JMatPro was used to predict the phases present during solidification and the approximate compoisitons for each phase are shown in Table 7. While the aluminum sample was molten during XRF measurements (based on temperature measurements and visual observation), the melt surface is cooler than the bulk , see Figure 7. Were the absolute surface cooler than our near surface measurements, solidification and settling of alpha and AlFeSi-beta could reduce the surface silicon concentration. Such silicon depletion would reduce the silicon XRF peak height.

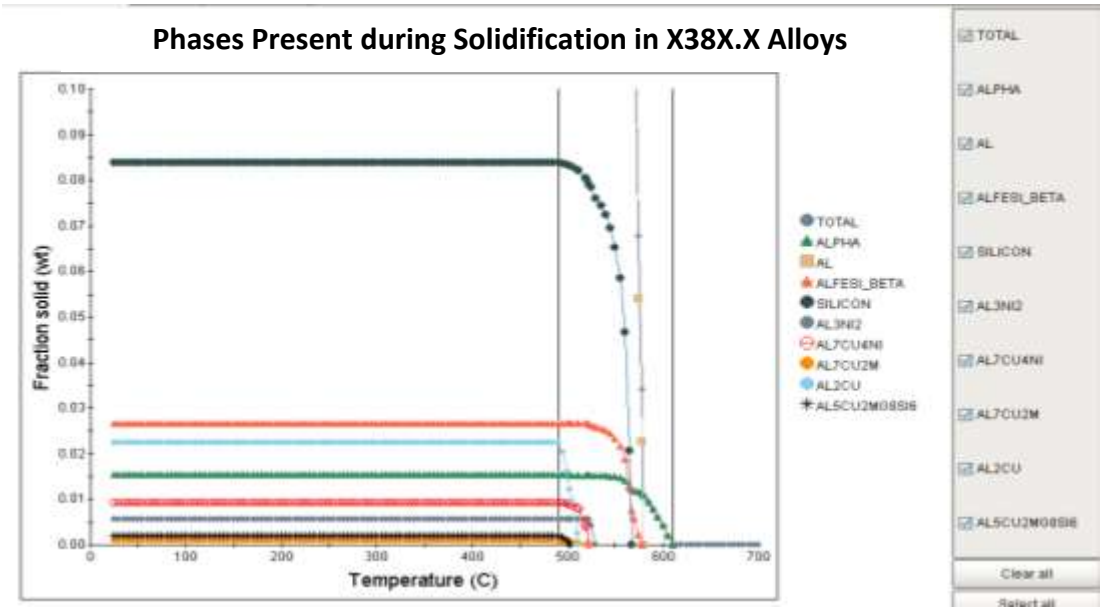

Figure 28: Fraction solid of phases present during solidification for the MMM alloys

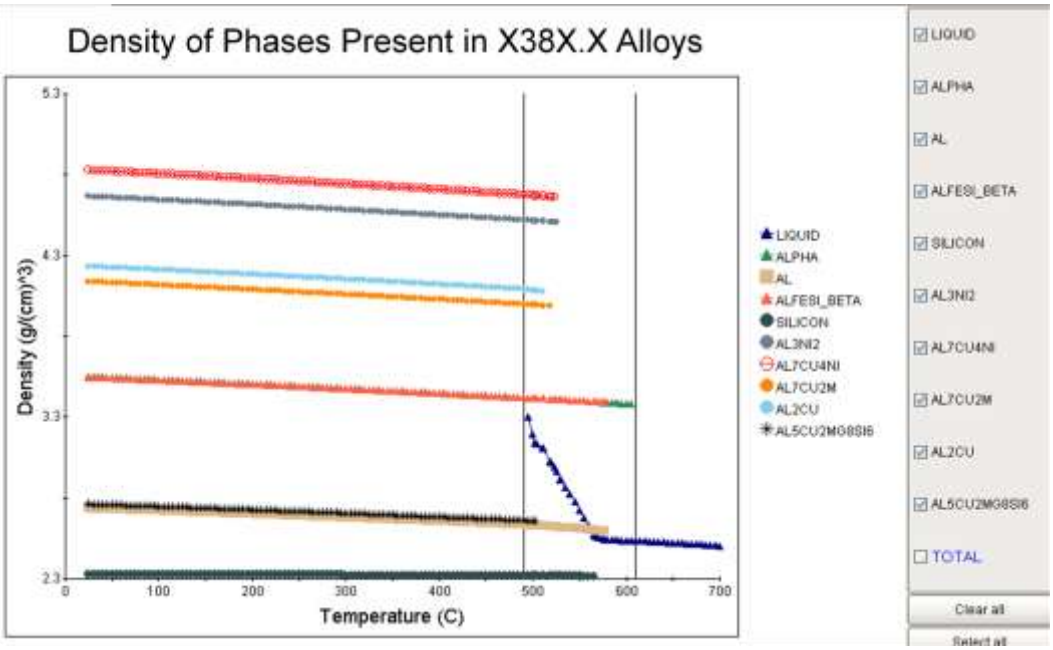

Figure 29: Density of phases present in MMM as a function of temperature

Table 7: Phase detail for MMM phases

Phase Details for X38X.X Phases			
Phase	**Temperature at which it forms (^{o}C)**	**Elements Present (wt%)**	**Approximate Density at which it forms(g/cm^3)**
Liquid Density before Solidification = 2.5			
Alpha	615	Al: 62% Fe: 18 Si: 8 Cu: 1 Mn: 11	3.4
Al	580	Al: 97% Fe: <1 Si: 1 Cu: 2 Zn: <1 Mg: <1 Mn: <1 Ni: <1 Sn: <1	2.7
AlFeSi Beta	573	Al: 58% Fe: 28 Si: 14	3.4
Si	567	Si Solid Solution	2.3
Al_3Ni_2	531	Al: Ni:	4.6
Al_7Cu_4Ni	511	Al: Cu: Ni:	4.7
Al_7Cu_2M	473	Al: 51% Cu: 34 Fe: 15	4.1
Al_2Cu	437	Al: 46% Cu: 54	4.2
$Al_5Cu_2Mg_8Si_6$	340	Al: 22% Cu: 20 Mg: 31 Si: 27	2.7

The spectra also show a sharp increase (2X) in silicon at the surface following solidification. This effect can most likely be attributed to the presence of silicon rich phases at the surface of the sample after melting. Micrographs are shown in Figure 30 and Figure 31 of an MMM sample after solidification. The sample was prepared with Keller's etchant and examined under polarized light. These micrographs show that no heavy oxidation occurred at the surface. However, there is non-uniformity in the structure from the surface to the bulk. The surface structure has a higher proportion of elongated script like

phases (most likely intermetallics) compared to the otherwise dendritic structure below the surface. Below the surface, the structure is dendritic with a light globular, most likely Si rich phase, within the interdendritic regions.

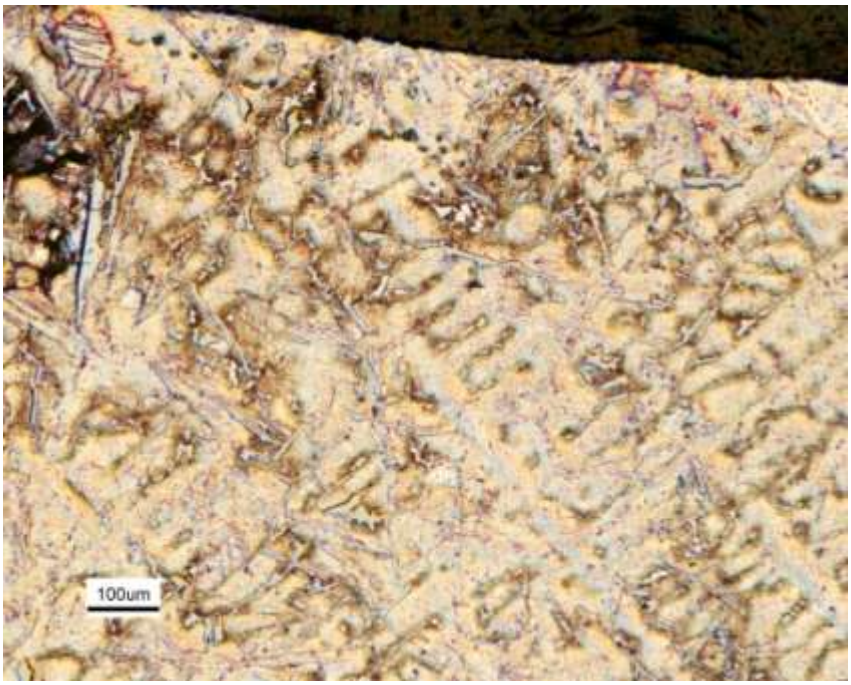

Figure 30: Low magnification micrograph of an MMM sample after melting revealing the microstructure at the top surface

Figure 31: High magnification micrograph of an MMM sample after melting revealing the microstructure at the top surface

6. Conclusions

In this work, laboratory equipment for molten metal XRF measurements was developed. The equipment provides a stable atmosphere for data acquisition to minimize oxidation of the sample and effectively protects the X-Ray tube and detector from excessive temperatures. Data acquisition settings for XRF spectra were established for this work and for future ATP work. A MatLab routine was written to analyze the data and provide the area under the curve for the peaks of interest. The MatLab routine was used to study the repeatability of spectra for the equipment and was shown to follow a normal distribution. Molten aluminum spectra were successfully acquired and differences were observed between solid and liquid spectra in all cases. The reason for the differences is not yet known, but hypotheses were made as to surface segregation, the Debye-Waller factor, and possible surface solidification of dense silicon bearing phases.

6.1. Recommendations for Further Work

In the future for this program, it is recommended that the constants needed for the fundamental parameters approach are determined for quantitative analysis. The MatLab routine showed that data was repeatable and peaks of interest were discernable, and so with that understanding it is recommended that the data be analyzed by commercial software that incorporates fundamental parameters such as capturing the primary spectrum for use in quantitative analysis. The calibration curve for this matrix must be developed and so it is important that the interelement effects, such as absorption and enhancement, are further studied for the X38X.X matrix to better understand the calibration curve. Interelement effects should be further investigated by completing Half Fraction Factorial and studying the interactions. Upon completion of the fraction factorial under pristine conditions, it would be of interest to study the effects of oxidation on the sample by perturbing the atmosphere to known concentrations of oxygen and determining if oxidation has a predictable effect on the spectra. This knowledge would be useful for the commercial application of this technology as oxidation to some degree will inevitably be present. It is important to continue to create hypotheses and investigate possible differences in the liquid and solid surfaces that may be causing the differences observed between the two as there is no literature so far on this topic. It would also be of interest in further work to investigate modifications to the equipment that would allow for isothermal measurements. The interaction between the EM field and the detector is not fully understood and so a modification to the current shielding or a new type of detector could be solutions to obtaining isothermal measurements. Isothermal measurements would allow for a more refined study on the effect of liquid temperature on XRF spectra, possibly revealing a temperature effect. Upon the completion of the recommended work, it is expected that the XRF spectra for liquid aluminum will be well understood by the ATP team and data fusion between XRF and LIBS can begin to create a precise and accurate system for on-line measurement of molten aluminum.

7. Appendices

A. Radiation Hazards in Spectrometry

The reader who wishes to learn more about radiation hazards in spectrometry should refer to the following sources:

1. Jenkins, R., R.W. Gould, and D. Gedcke. Quantitative X-Ray Spectrometry. New York: Marcel Dekker, Inc., 1995. Chapter 12: pp.429-438
2. *Radiation Safety for X-Ray Diffraction and Fluorescence Analysis Equipment*, N.B.S. Handbook III, American National Standard N43.2. 1971.
3. *Radiological Health Handbook*, U.S. Department of Health, Education, and Welfare, Washington, D.C., January 1970.

B. Specification Sheets for Experimental XRF Spectrometer

RoHS / WEEE Compliance X-ray Detector

X-RAY DETECTOR

XR-100CR

No Liquid Nitrogen
Solid State Design

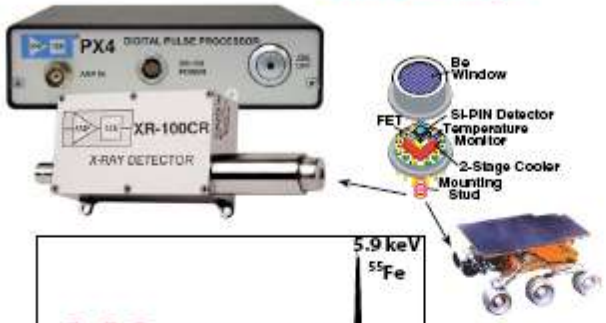

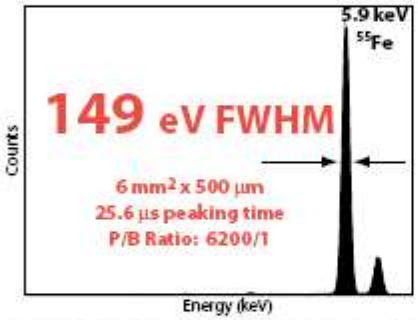

Resolution vs. ICR for Different Peaking Times

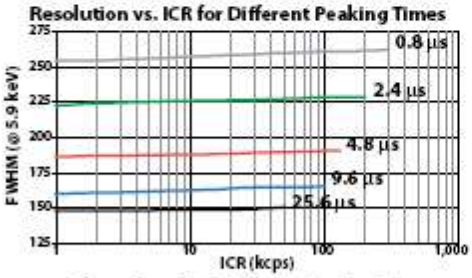

Throughput for Different Peaking Times

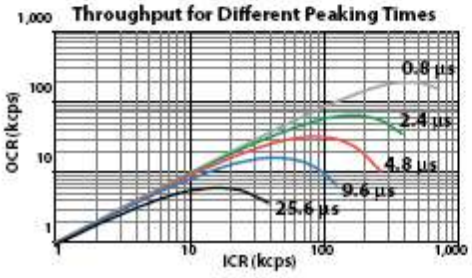

High Performance at Low Cost

FEATURES

- Si-PIN Photodiode
- Thermoelectric Cooler
- Beryllium Window
- Hermetic Package (TO-8)
- Wide Detection Range
- Easy to Operate

APPLICATIONS

- X-Ray Fluorescence
- OEM
- Process Control
- Portable Instruments
- Art & Archaeology
- Teaching & Research
- Lead Detectors
- Space and Astronomy
- Environmental Monitoring
- Nuclear Plant Monitoring
- Heavy Metals in Plastic
- Semiconductor Processing
- Plating Thickness
- Sulfur in Oil & Coal Detection
- Smoke Stack Analysis
- Coal & Mining Operations
- Jewelry Analysis
- Forensic Investigations

Model *XR-100CR* is a high performance X-Ray Detector, Preamplifier, and Cooler system using a thermoelectrically cooled Si-PIN Photodiode as an X-Ray detector. Also mounted on the 2-stage cooler are the input FET and a novel feedback circuit. These components are kept at approximately -55°C, and are monitored by an internal temperature sensor. The hermetic TO-8 package of the detector has a light tight, vacuum tight thin Beryllium window to enable soft X-Ray detection.

Power to the XR-100CR is provided by either the PX2CR or the PX4. The PX2CR is AC powered and includes a spectroscopy grade Shaping Amplifier with fixed time constant (6 µs, 12 µs, or 20 µs). The PX4 is DC powered by an AC adaptor and provides both a variable Shaping Amplifier (.25 µs to 40 µs) and the MCA function.

The XR-100CR/PX2CR or XR-100CR/PX4 system ensures stable operation in less than one minute from power turn-on.

The resolution for the 5.9 keV peak of ^{55}Fe is 145 eV FWHM to 260 eV FWHM depending on the detector type and shaping time constant (see next page for selection guide).

SPECIFICATIONS

GENERAL	
Detector Type	SI-PIN
Detector Size	5 mm^2 to 20 mm^2. See Selection Guide.
Silicon Thickness	300 µm, 500 µm, 680 µm
Energy Resolution @ 5.9 keV, ^{55}Fe	145 eV FWHM to 260 eV FWHM depending on detector type and shaping time constant. See Selection Guide.
Background counts	<3 x 10^{-3} /s, 2 keV to 150 keV for 7 mm^2 / 300 µm detector
Be Window	1 mil (25 µm), or 0.5 mil (12.5 µm) thick
Charge Sensitive Preamplifier	Amptek custom design with reset though the H.V. connection
Case Size	3.75 x 1.75 x 1.13 in (9.5 x 4.4 x 2.9 cm)
Weight	4.4 ounces (125 gm)
Total Power	<1 Watt
Warranty Period	1 year
Typical Lifetime	5 to 10 years, depending on use
Storage Time	10+ years in dry environment
Operation Conditions	0°C to +40°C
OPTIONS	
Detector sizes from 5 mm^2 to 20 mm^2 (300 µm to 680 µm thick). See Selection Guide.	
Other Beryllium window thicknesses are available on special order (0.3 mil - 7.5 µm).	
See also XR-100T-CdTe specifications using Cadmium Telluride (CdTe) diode detectors for high efficiency and high resolution Gamma Ray detection (<1 keV FWHM @ 122 keV, ^{57}Co).	
Collimator Kit for high flux applications.	
INPUTS	
Preamp Power	±8 to 9 V @ 15 mA with <50 mV peak-to-peak noise.
Detector Power	+100 to +200 V @ 1 µA depending on detector type; <0.1% variation.
Cooler Power	Current = 350 mA maximum Voltage = 4 V maximum with <100 mV peak-to-peak noise Internal temperature controller
OUTPUTS	
Preamplifier Sensitivity Polarity Feedback	 1 mV/keV typical (may vary for different detectors) Negative Signal Out, 1 kΩ maximum load Reset through the detector capacitance
Temperature Monitor Sensitivity	PX2CR: 770 mV = -50 °C with diode PX4: direct reading in K through software

CONNECTORS	
Preamp Output	BNC coaxial connector
Power and Signal	6-Pin LEMO connector (Part #ERA.1S.306.CLL)
Interconnect Cable	To PX2CR: 6-Pin LEMO (Part #FFA.1S.CLAC57) 9-Pin D (5 ft length). To PX4: 6-Pin LEMO (Part #FFA.1S.306.CLAC57) to 6-Pin LEMO (5 ft length).
6-PIN LEMO CONNECTOR	
Pin 1	Temperature monitor, AD590 or Diode
Pin 2	+ H.V. Detector Bias, +100 - 200 V maximum
Pin 3	-9 V Preamp Power
Pin 4	+9 V Preamp Power
Pin 5	Cooler Power Return
Pin 6	2-Stage Cooler Power: 0 to +3 V @ 350 mA
CASE	Ground and Shield

AMPTEK XR-100CR Selection Guide

Detector System Area/Thickness Be Window Thickness	Typical Energy Resolution eV FWHM @ 5.9 keV with 25.6 µs Peaking Time (PX4)* Peak to Background Ratio (P/B)**
The following detectors contain either a Silver (Ag) or Multilayer Internal Collimator:	
XR-100CR 5 mm2 / 500 µm or 680 µm 0.5 or 1.0 mil Be	145 - 175 eV P/B: 1100/1 for 500 µm thick 1500/1 for 680 µm thick
XR-100CR 6 mm2 / 500 µm 0.5 or 1.0 mil Be	145 - 175 eV P/B: 6200/1
XR-100CR 13 mm2 / 500 µm 1.0 mil Be	190 - 200 eV P/B: 4100/1
XR-100CR 20 mm2 / 680 µm 1.0 mil Be	20 µs: 200 - 240 eV P/B: 1100/1
The following detectors are partially depleted and contain no internal collimator:	
XR-100CR 7 mm2 / 300 µm 0.5 or 1.0 mil Be	165 - 185 eV P/B: 250/1 (5000/1 with external collimator)
XR-100CR 13 mm2 / 300 µm 0.5 or 1.0 mil Be	200 - 220 eV P/B: 550/1 (4000/1 with external collimator)

*Peaking time is approximately 2.4 x shaping time.
**The Peak to Background (P/B) Ratio is the ratio of the counts at the 5.9 keV peak to the counts at about 2 keV

For full system specifications, please see http://www.amptek.com/xr100cr.html

Digital Pulse Processor and Power Supply

PX4

Features

- Single unit compatible with all Amptek XR100 Si and CdTe detectors, includes:
  - ❖ Shaping amplifier using the DP4 digital pulse processing technology
  - ❖ Integrated multichannel analyzer
  - ❖ Power supplies
- Can be used with detectors from other manufacturers
- Trapezoidal shaping with wide range of shaping time settings to optimize performance
- High count rate capability with excellent baseline stability, throughput, and pile-up rejection
- Up to 8 k output MCA channels
- USB interface to personal computer, with software to support instrument control, data acquisition, and analysis
- Oscilloscope mode available - DAC output for pulse monitoring and adjustment

Power

- High voltage bias adjustable 100V to 1.5 kV
- Thermoelectric cooler with feedback
- Operates from AC supply

FRONT

BACK

Photograph of the front and back of the PX4.

Physical

- Low Power: 2 W typical
- Small Size: 6.5 x 5.5 x 1.5 inches
  165 x 135 x 40 mm
- Light Weight: 1.6 lbs/750 g

Overview

The Amptek PX4 is an interface between Amptek's XR100 series of X-ray and γ-ray detectors and a personal computer with data acquisition, control, and analysis software. The PX4 includes three major components: (1) a shaping amplifier, based on a state of the art, high performance, low power DP4 digital pulse processor, (2) a multichannel analyzer, and (3) power supplies. It replaces both the previous generation PX2 shaping amplifier and power supply and the separate MCA.

The pulse processing and MCA function of the PX4 are based on Amptek's DP4 digital pulse processor. The PX4 offers several performance advantages over traditional analog systems, including higher energy resolution, reduced ballistic deficit, higher throughput, better pile-up rejection, enhanced stability, and the ability to adjust shaping time parameters over a wide range to optimize performance. The PX4 includes a USB interface. The power supply portion of the PX4 provides all of the power necessary for the detector, preamplifier, and the PX4.

The PX4 offers several advantages over the previous generation PX2: (1) a single unit interfaces with all XR100 variants; (2) many parameters may be adjusted to optimize performance, such as shaping time constant and HV bias; (3) the pulse processor offers enhanced baseline stability, throughput, pile-up rejection, and Rise Time Discrimination (RTD); and (4) the MCA is integrated with the complete system.

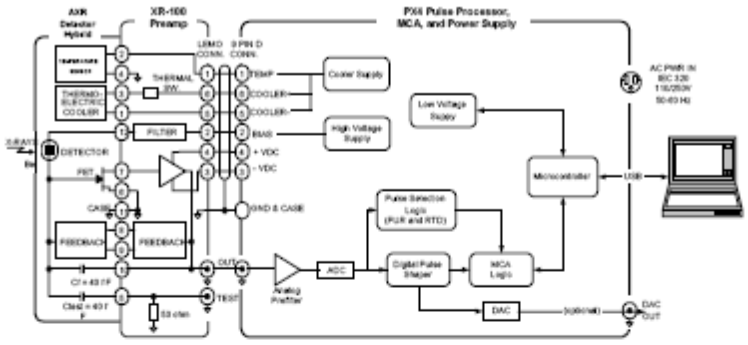

Figure 1. Block diagram of the PX4 in a complete system.

The signal input to the PX4 is the preamplifier output. The PX4 digitizes the preamplifier output, applies real-time digital processing to the signal, detects the peak amplitude (digitally), and bins this value in its histogramming memory, generating an energy spectrum. The use of digital signal processing offers several important performance advantages compared to previous systems. The spectrum is then transmitted over the PX4's USB interface to the user's computer. The PX4 hardware is controlled over the USB interface, permitting the user not only to start and stop acquisition but to select shaping times, select the HV bias, etc.

Specifications

Gain Settings: 28 user selectable gain settings from x4 to x550. Fine gain is adjustable between 0.75 and 1.25.

Pulse Shape: Trapezoidal. A semi-gaussian amplifier with shaping time τ has a peaking time of 2.2τ and is comparable in performance with the trapezoidal shape of the same peaking time.

Peaking and Flat Top Times: Twenty-four programmable peaking times between 0.8 and 102 µsec. For each peak time, sixteen flat top durations are available, > 0.2 µsec

Rise Time Discriminator (RTD): The digital pulse processor can be programmed to select input pulses based on their rise time properties.

Throughput: The pulse processing electronics have a cycle time of 1 µsec. With a peaking time of 0.8 µsec, a 1MHz periodic signal can be acquired. Dead time is 1.25 x peaking time.

Pile-Up Reject: Pulses separated by more than the fast channel resolving time, 600 nsec, and less than 1.25 x peaking time are rejected.

Number of channels: Commandable to 256, 512, 1 k, 2 k, 4 k or 8 k channels.

Connections

Analog Input (BNC): The analog input accepts pulses from the XR100 or any other detector with preamplifier reset or resistive feedback.

XR100 Power (6 pin LEMO): Provides power to preamp and detector. Includes HV bias, thermoelectric cooler power, and preamp power.

Serial Interface (USB): Standard USB interface and RS-232 interface to personal computer. Used for data acquisition and hardware control.

DAC Output (BNC): This output is used in oscilloscope mode, to view the shaped pulse and other diagnostic signals. Range: 0 to 1 V.

Input Power: 5 VDC (500 mA max) via power jack. It mates with a center positive 5.5 mm x 2.1 mm Power Plug.

For further technical specifications see our web site: www.amptek.com

AMPTEK Inc. 14 DeAngelo Dr Bedford MA 01730
Tel: +1 (781) 275-2242 Fax: +1 (781) 275-3470 email: sales@amptek.com www: http://www.amptek.com

C. Probability Plots for Repeatability of Spectra

The probability plots for each characteristic emission line of interest are presented here to show the normality of the spectra. Overall, the data follows a normal distribution and any deviations can most likely be attributed to the small sample size (n=20).

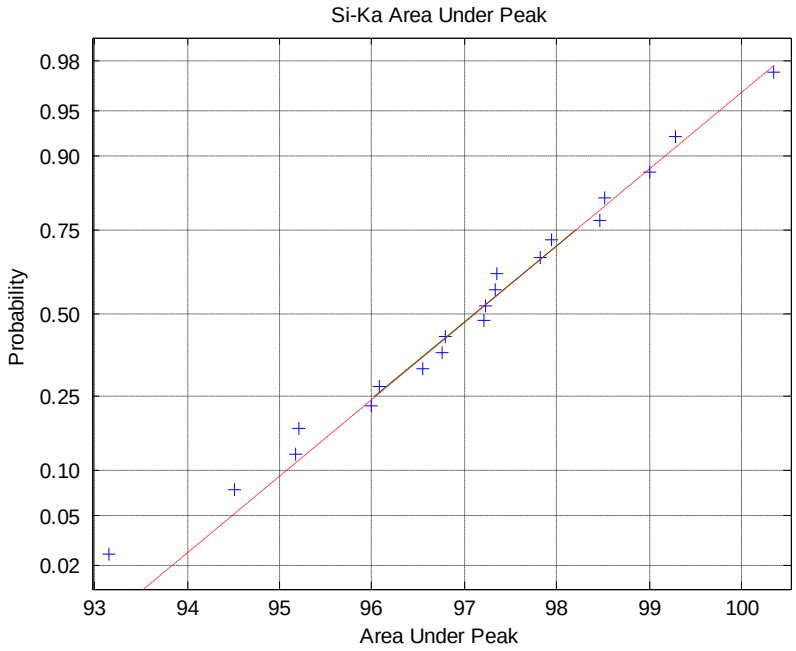

Figure 32: Normal probability plot for the area under the Si-Ka Peak for 20 Consecutive Trials

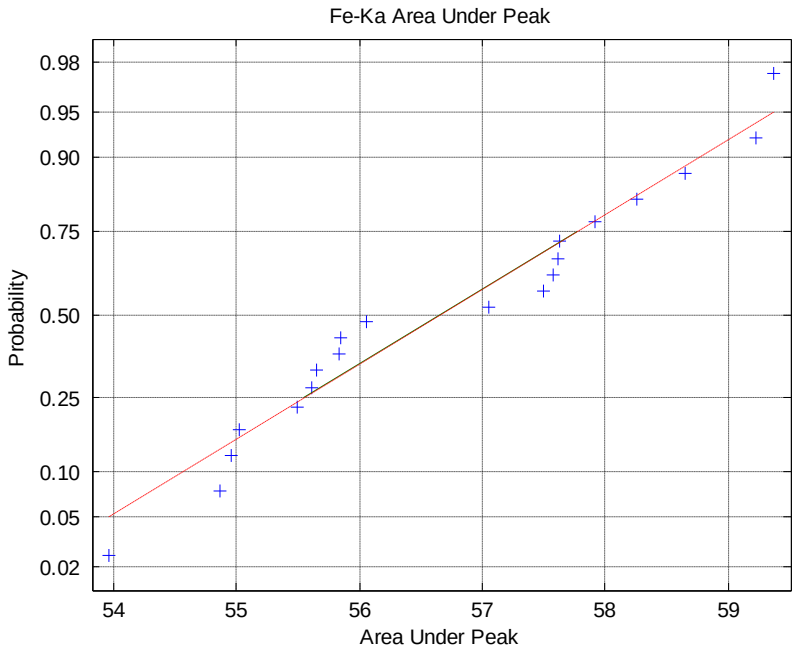

Figure 33: Normal probability plot for the area under the Fe-Ka Peak for 20 Consecutive Trials

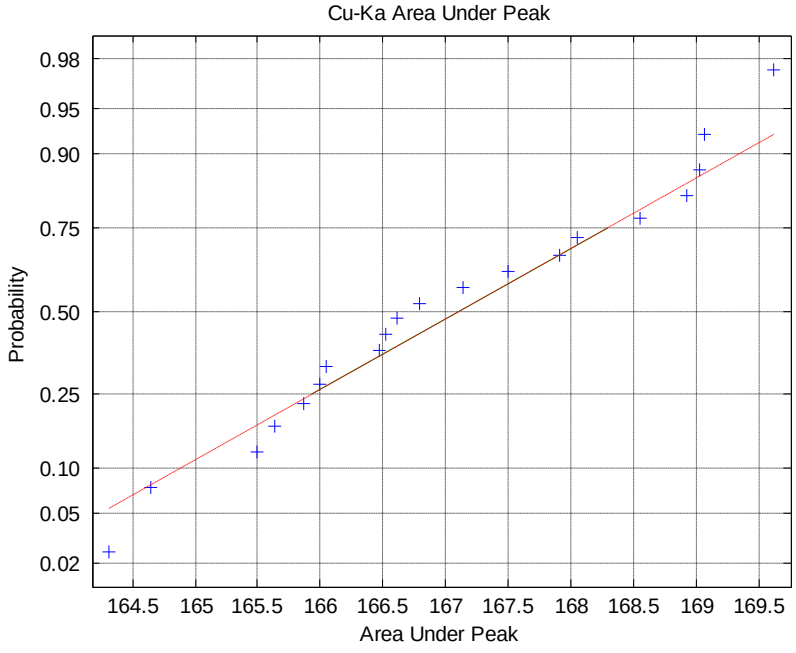

Figure 34: Normal probability plot for the area under the Cu-Ka Peak for 20 Consecutive Trials

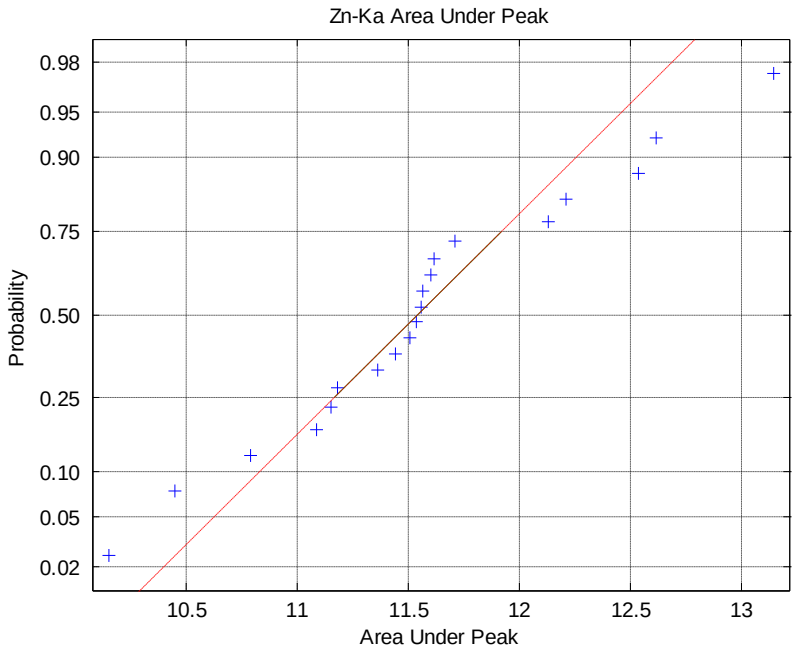

Figure 35: Normal probability plot for the area under the Zn-Ka Peak for 20 Consecutive Trials

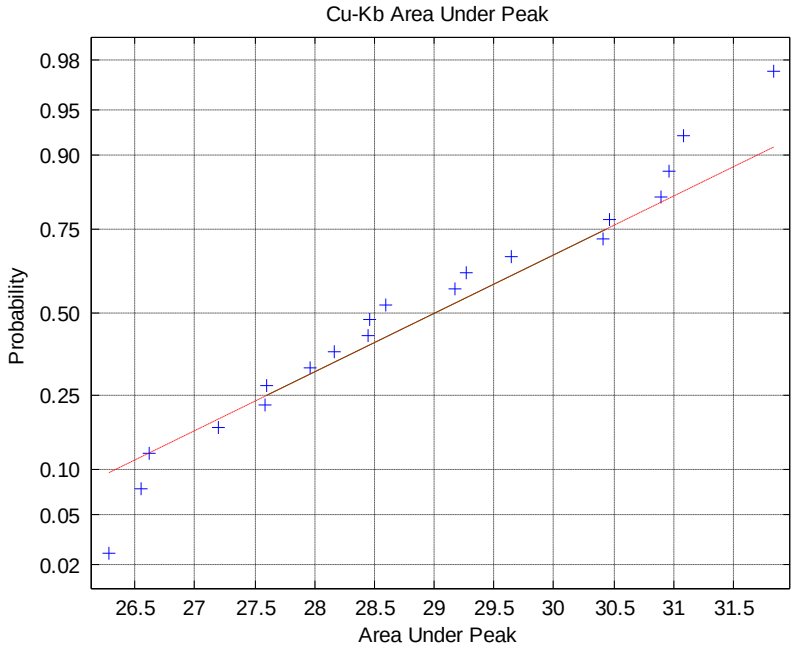

Figure 36: Normal probability plot for the area under the Cu-Kb Peak for 20 Consecutive Trials

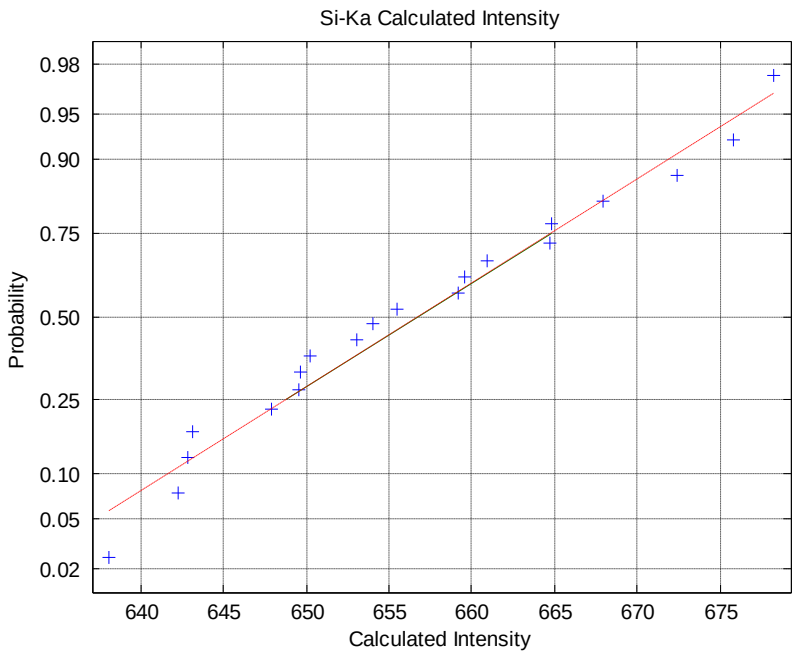

Figure 37: Normal probability plot for the calculated intensity of the Si-Ka Peak for 20 Consecutive Trials

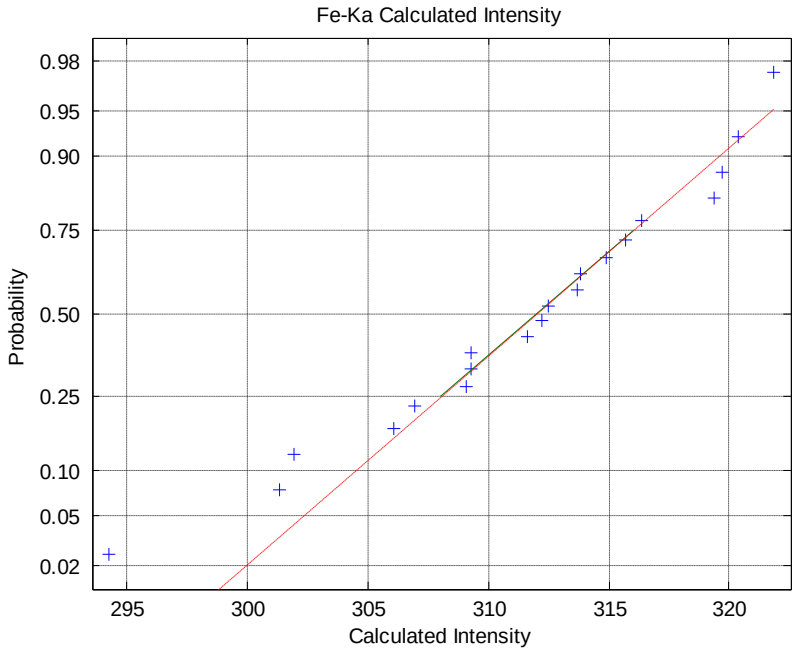

Figure 38: Normal probability plot for the calculated intensity of the Fe-Ka Peak for 20 Consecutive Trials

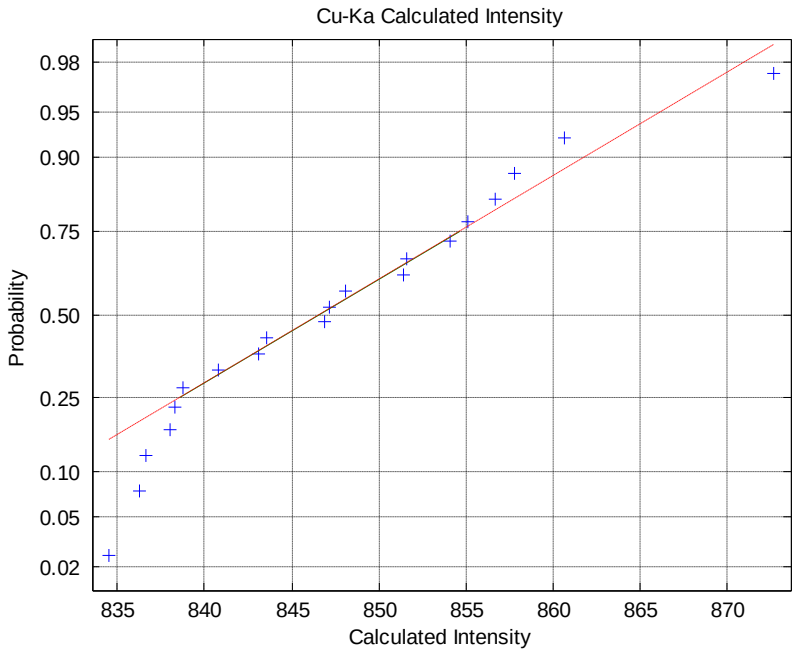

Figure 39: Normal probability plot for the calculated intensity of the Cu-Ka Peak for 20 Consecutive Trials

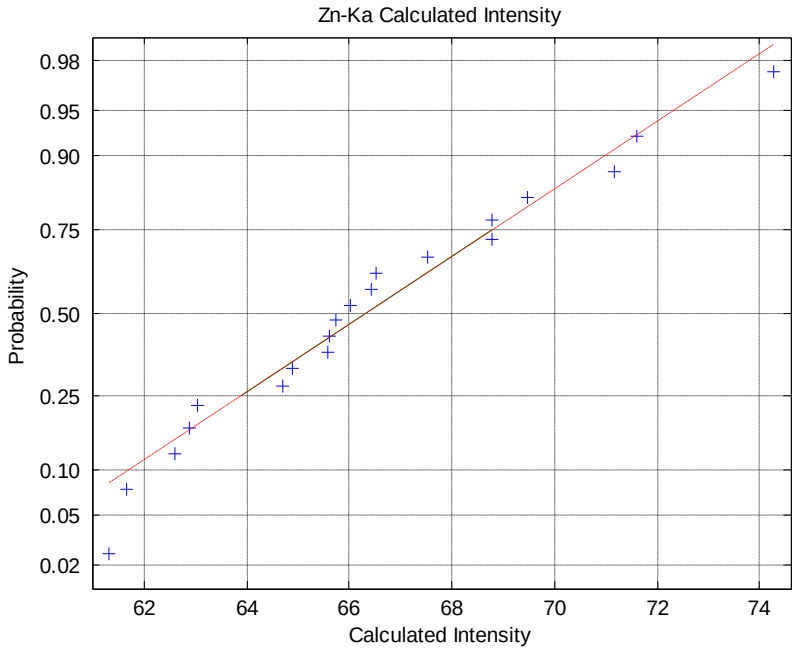

Figure 40: Normal probability plot for the calculated intensity of the Zn-Ka Peak for 20 Consecutive Trials

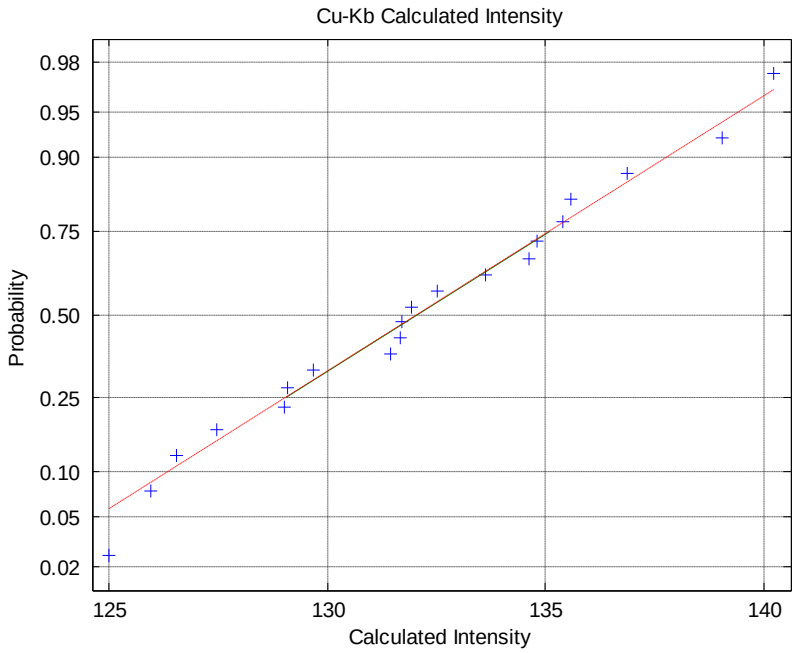

Figure 41: Normal probability plot for the calculated intensity of the Cu-Kb Peak for 20 Consecutive Trials

D. Mass Attenuation for the X38X.X Matrix

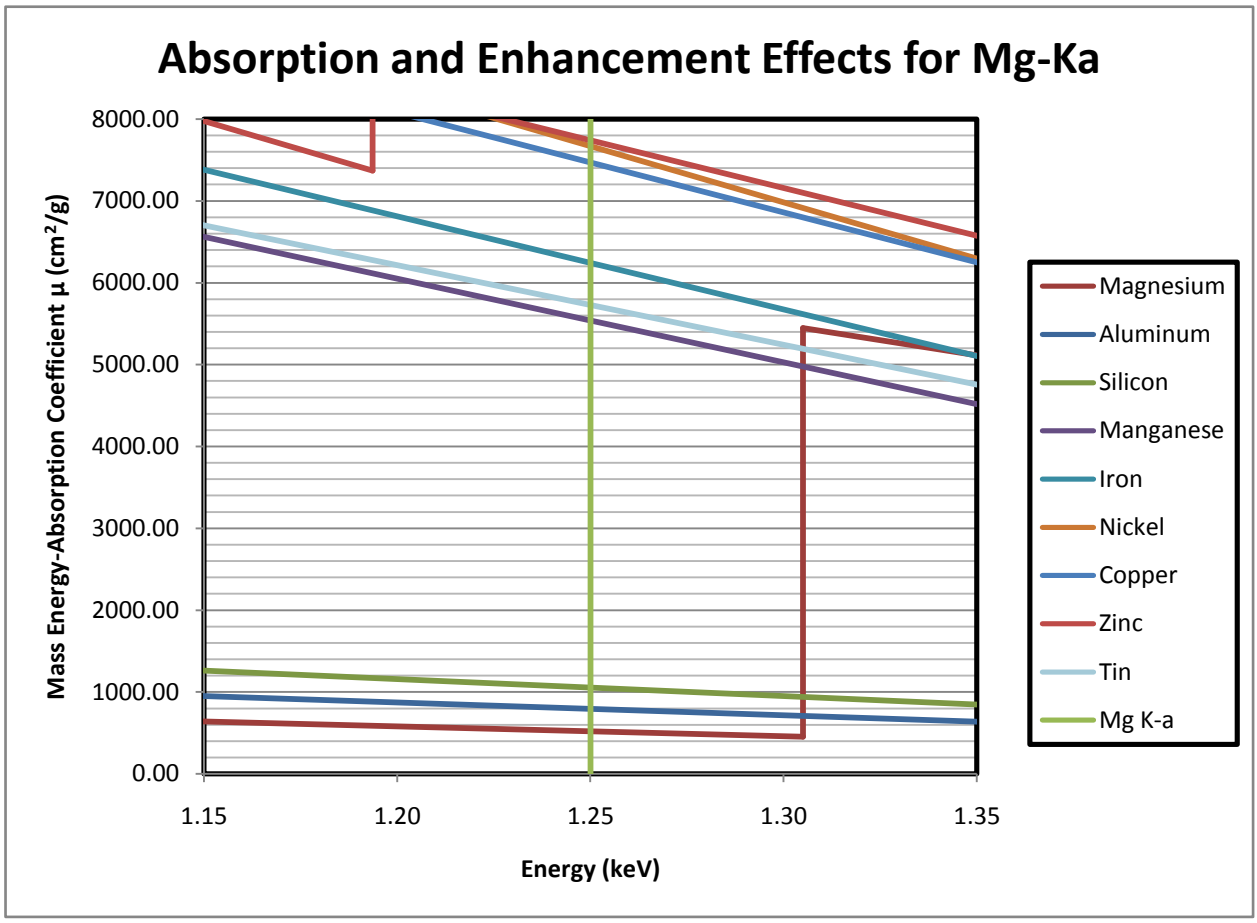

Figure 42: Absorption and Enhancement Effects for Mg-Ka

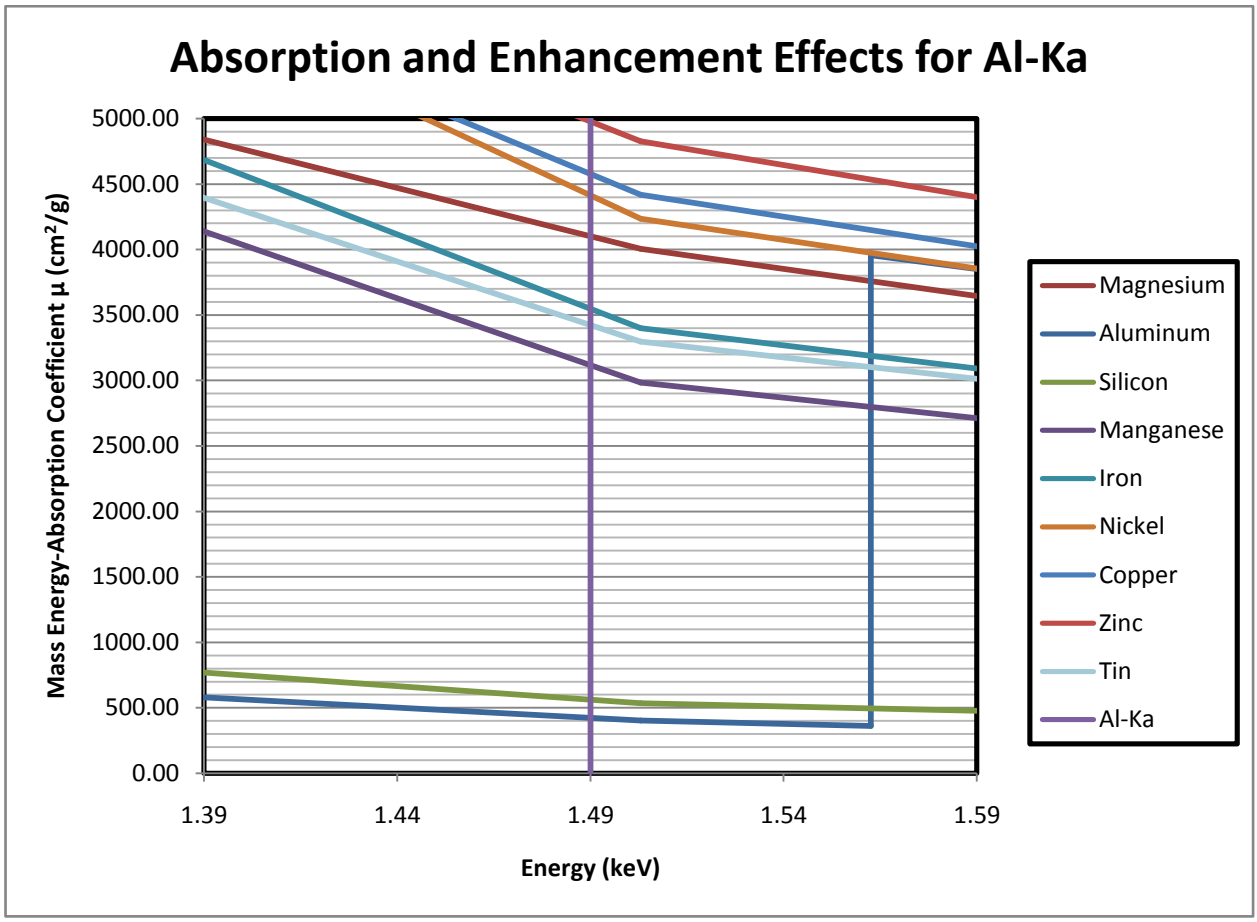

Figure 43: Absorption and Enhancement Effects for Al-Ka

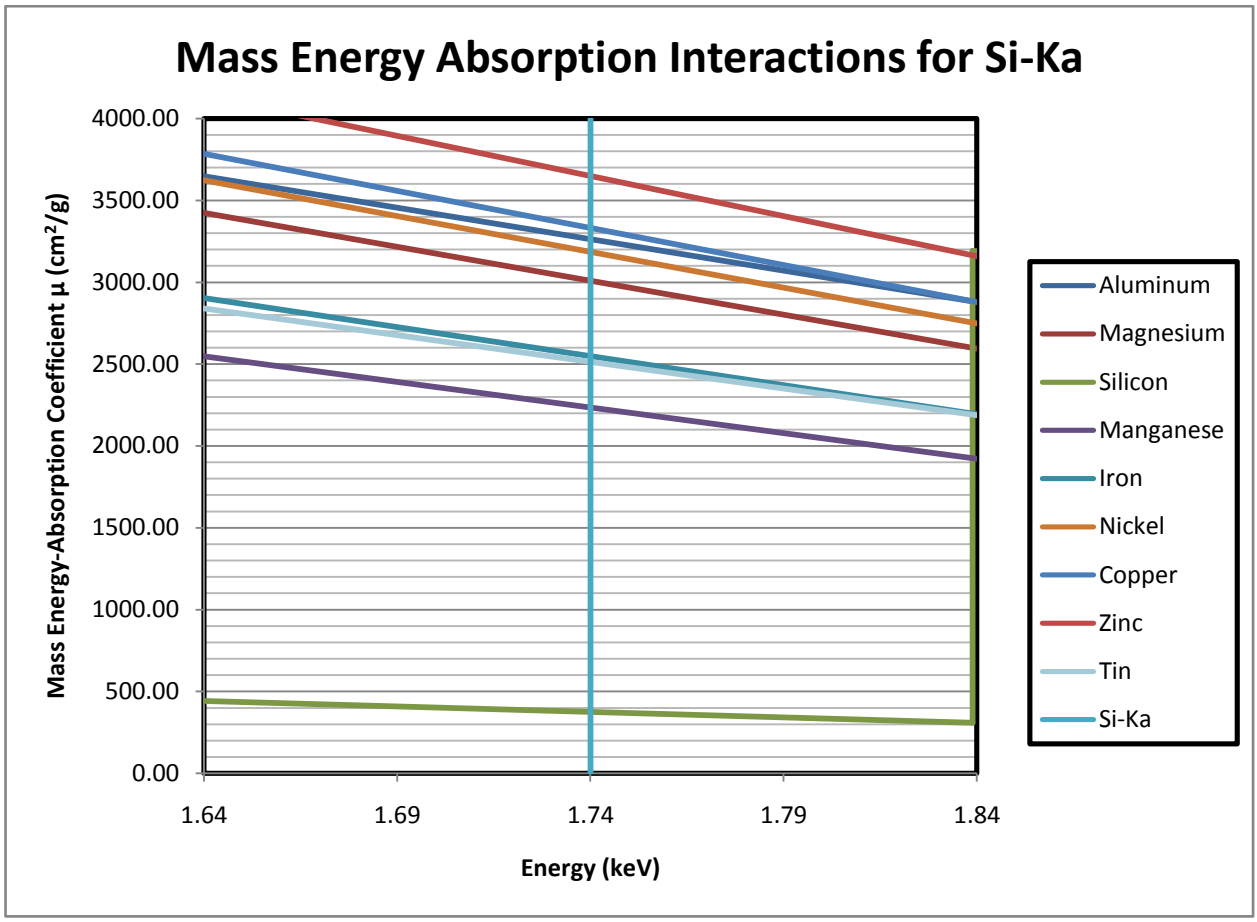

Figure 44: Absorption and Enhancement Effects for Si-Ka

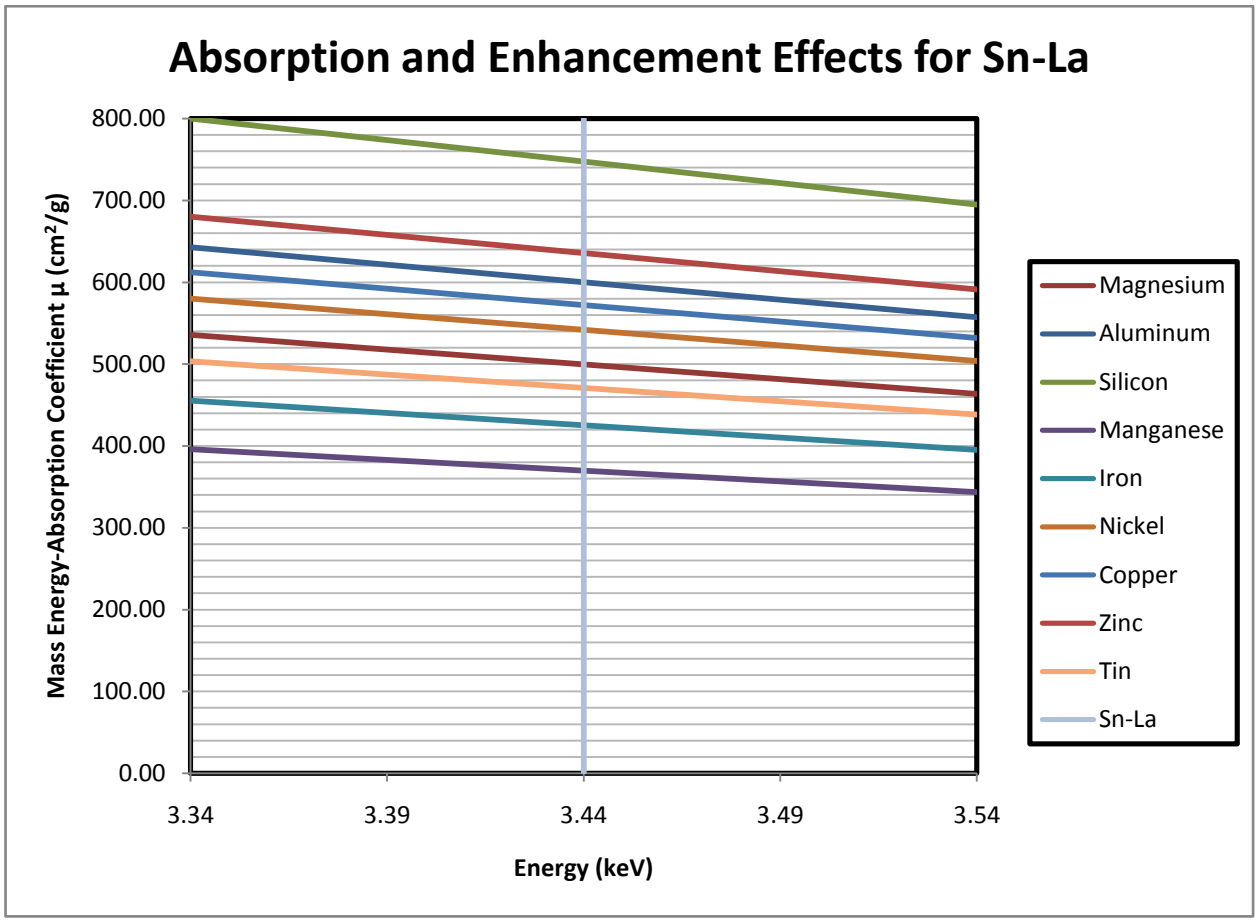

Figure 45: Absorption and Enhancement Effects for Sn-La

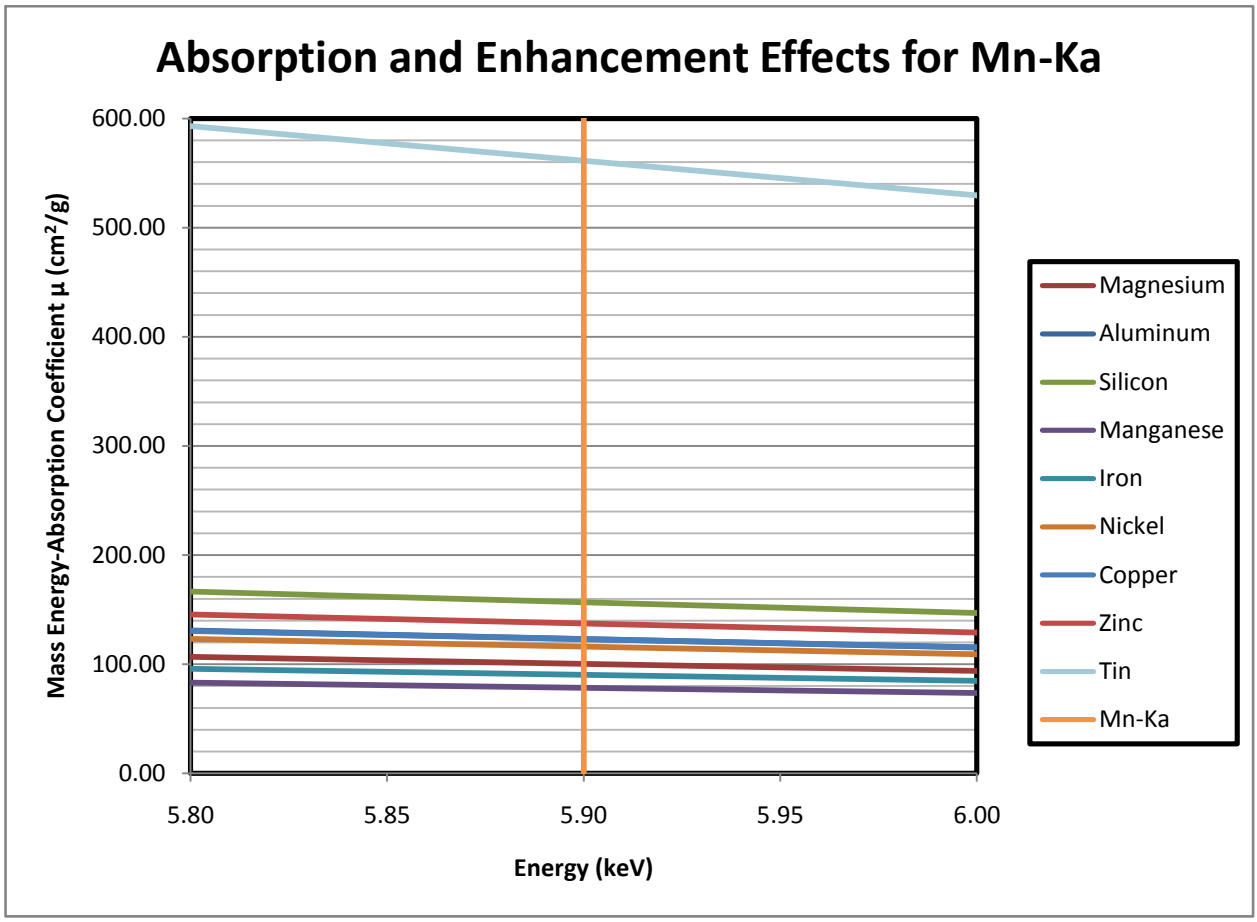

Figure 46: Absorption and Enhancement Effects for Mn-Ka

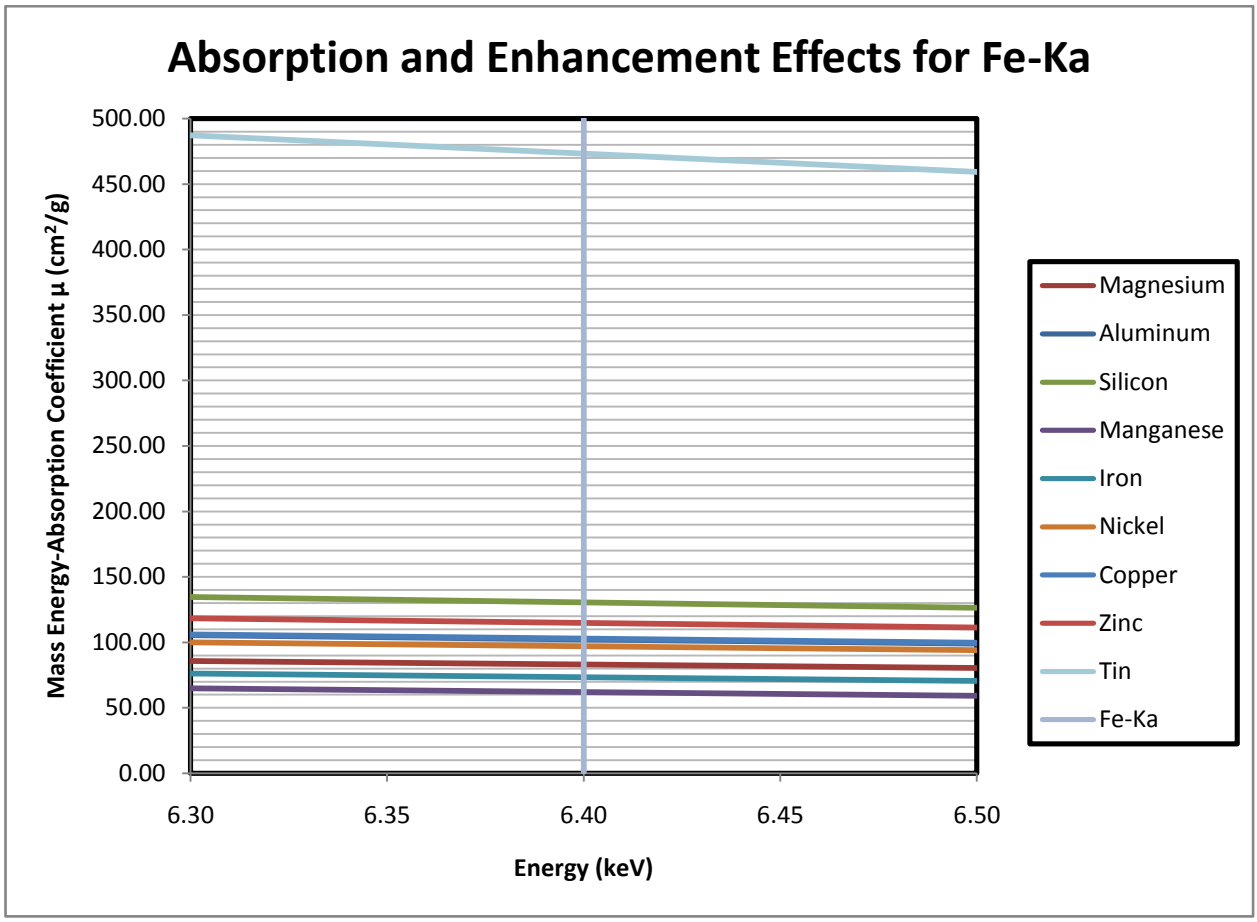

Figure 47: Absorption and Enhancement Effects for Fe-Ka

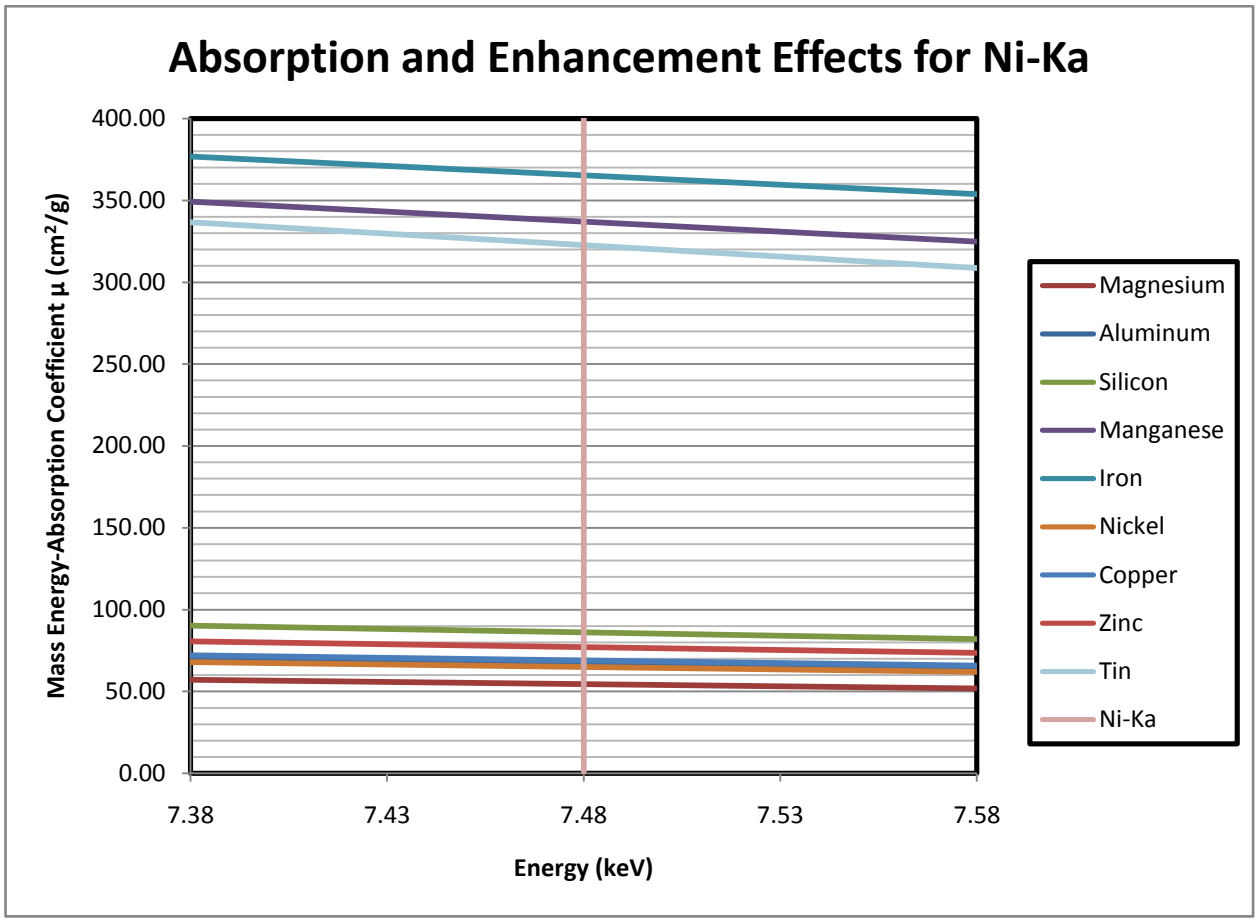

Figure 48: Absorption and Enhancement Effects for Ni-Ka

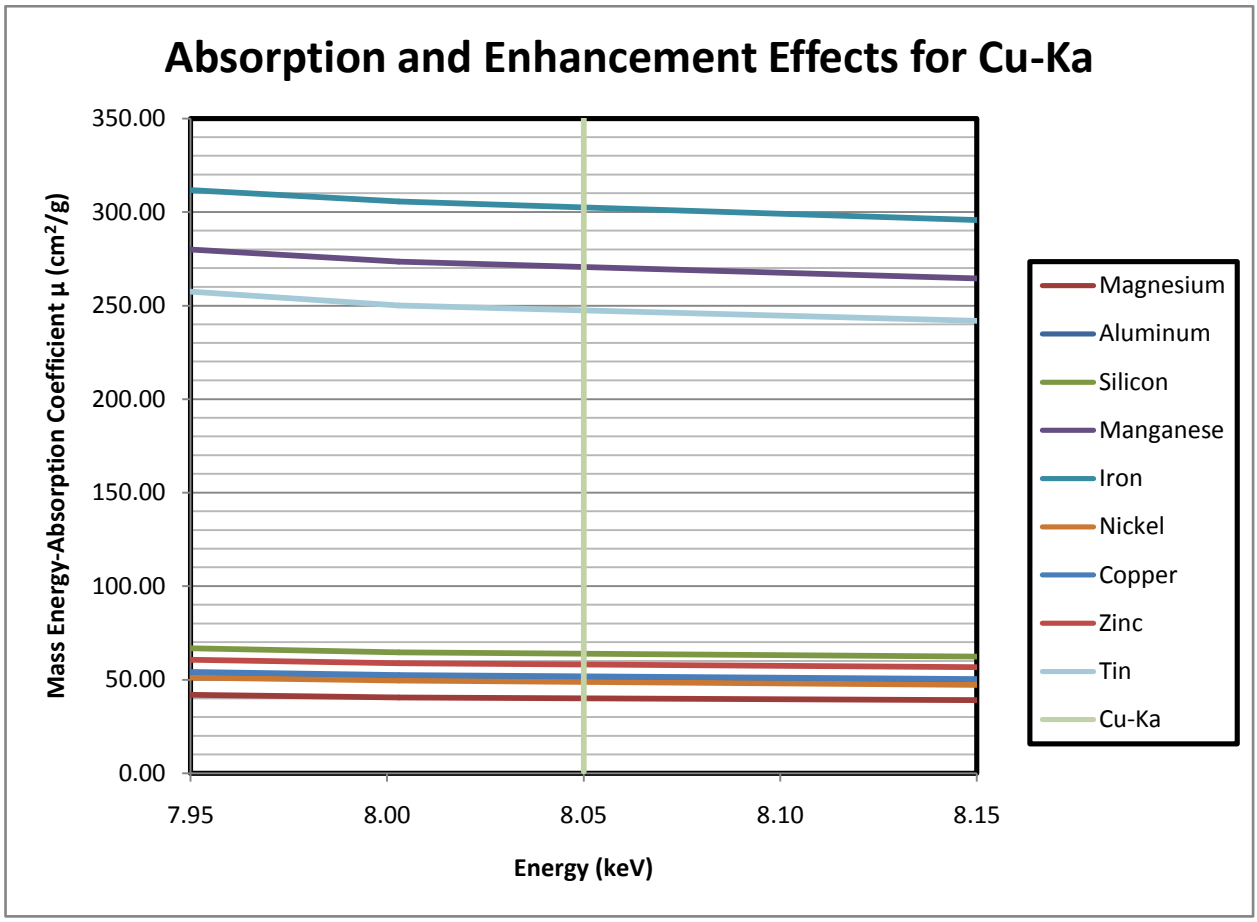

Figure 49: Absorption and Enhancement Effects for Cu-Ka

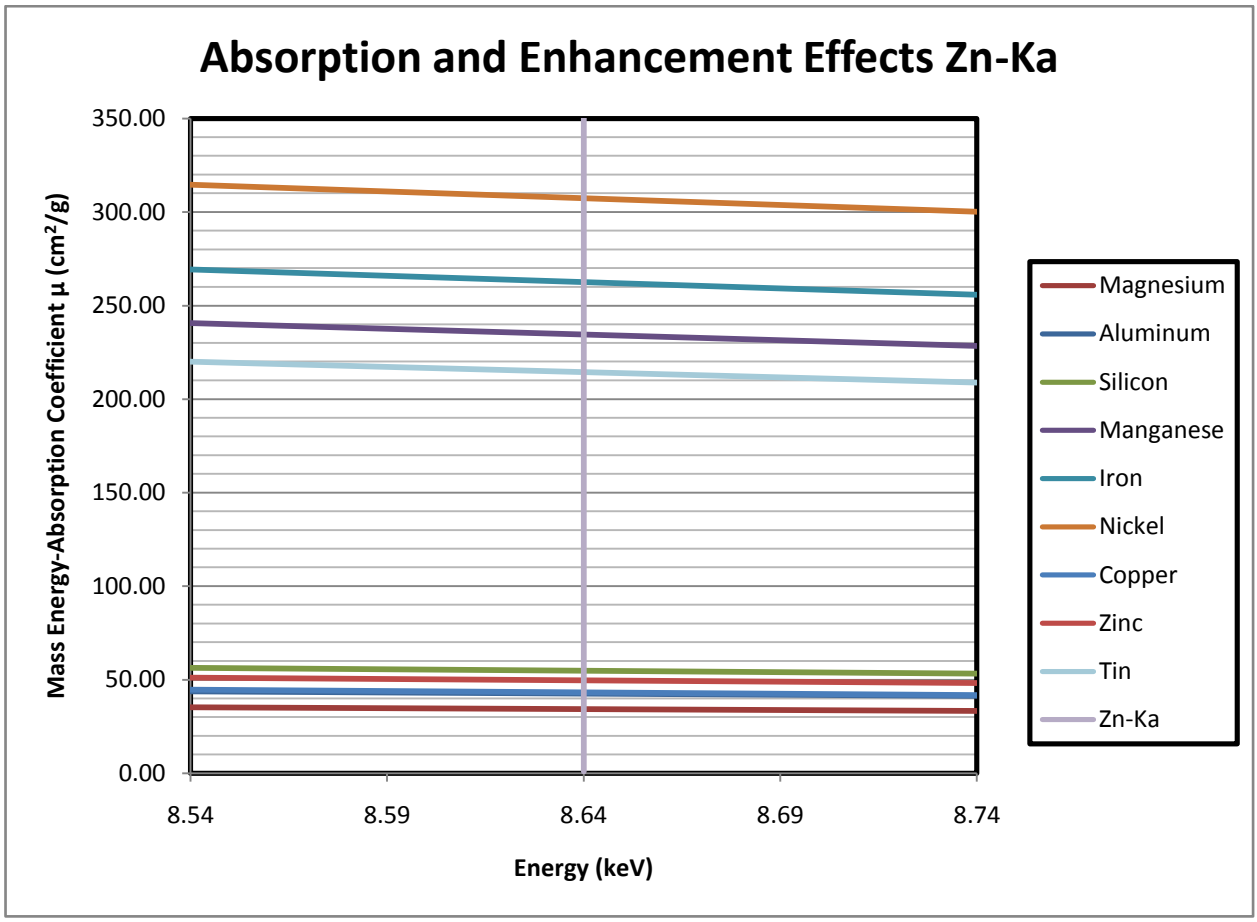

Figure 50: Absorption and Enhancement Effects for Zn-Ka

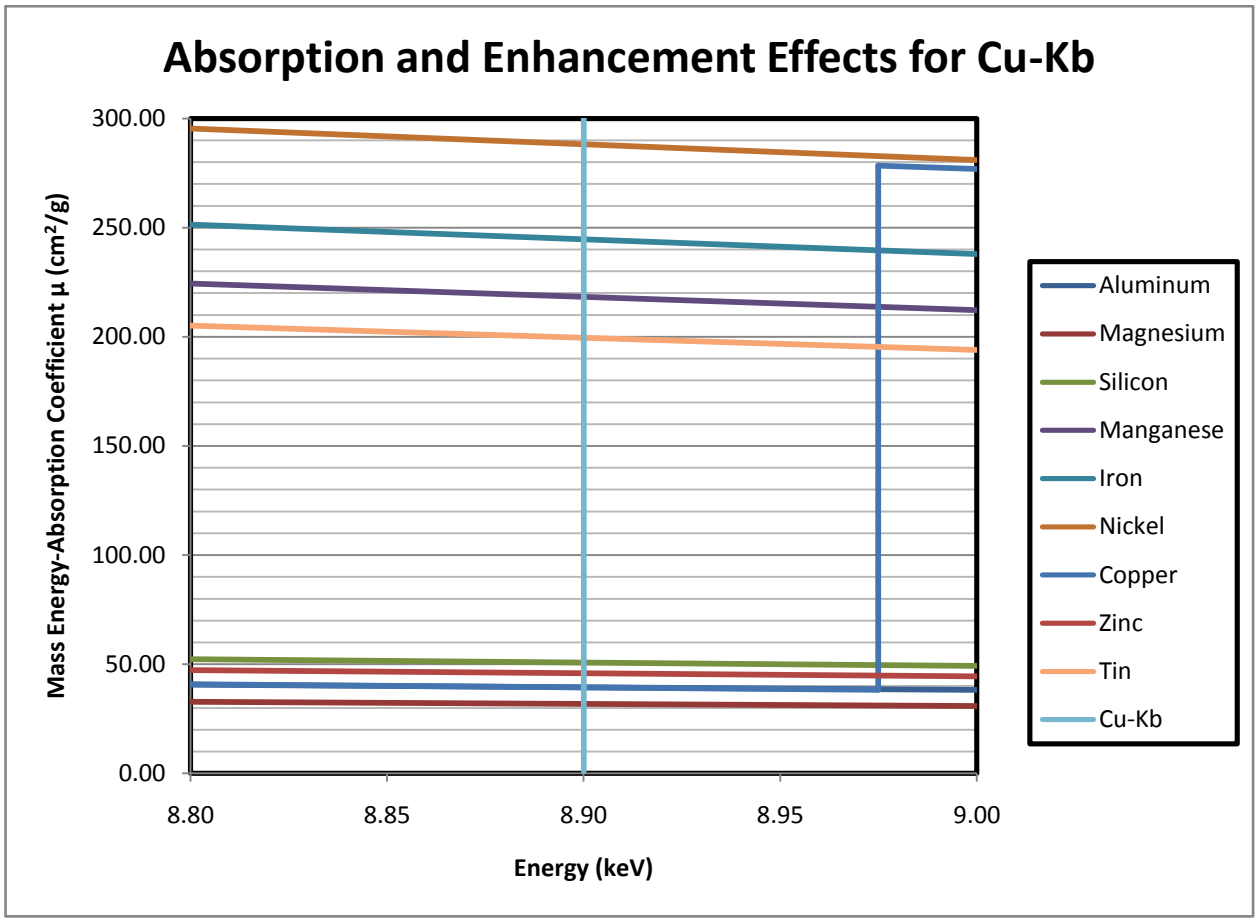

Figure 51: Absorption and Enhancement Effects for Mg-Ka

References

[1] Spencer, D.B.. "The High-Speed Identification and Sorting of Nonferrous Scrap." *JOM Journal of the Minerals, Metals and Materials Society* 57 (2007) 46-51.

[2] Das, S.K., J.A.S.Green, and J.G. Kaufman. "The Development of Recycle-Friendly Automotive Aluminum Alloys." *JOM Journal of the Minerals, Metals and Materials Society* 59 (2007) 47-51.

[3] Jenkins, R., R.W. Gould, and D. Gedcke. Quantitative X-Ray Spectrometry. New York: Marcel Dekker, Inc., 1995.

[4] Van Grieken, R.E., and A.A. Markowicz. Handbook of X-Ray Spectrometry. New York: Marcel Dekker, Inc., 2002.

[5] Creasy, L.E.. "On-Line Analysis of Molten Metals Using a Wavelength Dispersive X-Ray Spectrometer." *Advances in X-Ray Analysis* 37 (1994) 729-733.

[6] Paksy, L., B. Német, A. Lengyel, L. Kozma, and J. Czekkel. "Production control of metal alloys by laser spectroscopy of the molten metals Part 1. Preliminary investigations." *Spectrochimica Acta Part B* 51 (1996) 279-290.

[7] Gruber, J., J. Heitz, H. Strasser, D. Bäuerle, and N. Ramaseder. "Rapid in-situ Analysis of Liquid Steel by Laser-Induced Breakdown Spectroscopy." Spectrochimica Acta Part B 56 (2001) 685-693.

[8] Ria, K. A., F.Y Yueh, and J.P. Singh. "Laser-induced breakdown spectroscopy of molten aluminum alloy." *Applied Optics* 42 (2003) 2078-2084.

[9] **www.oxfordxtg.com**

[10] http://amptek.com/xr100cr.html

[11] Hubbell, J.H., and S. M. Seltzer. "Tables of X-Ray Mass Attenuation Coefficients and Mass Energy-Absorption Coefficients." Ionizing Radiation Division, Physics Laboratory National Institute of Standards and Technology: 1996. http://physics.nist.gov/PhysRefData/XrayMassCoef/cover.html

[12] Park, S.H., B.Y. Hur, S.Y. Kim, D.K. Ahn, and D.I. Ha. "A Study on the Viscosity and Surface Tension for Al Foaming and the Effects of Addition Elements." Proceedings of the 65th World Foundry Congress (2002) 515-524.

[13] Anson, J.P., R.A.L. Drew, and J.E. Gruzleski. "The Surface Tension of Molten Aluminum and Al-Si-Mg Alloy under Vacuum and Hydrogen Atmospheres." *Metallurgical and Materials Transactions B* 30 (1999) 1027-1032.